Postdeployment Calibration of a Tropical UHF Profiling Radar via Surface- and Satellite-Based Methods

LESLIE M. HARTTEN AND PAUL E. JOHNSTON

Cooperative Institute for Research in Environmental Sciences, University of Colorado Boulder, and Physical Sciences Division, NOAA/Earth System Research Laboratory, Boulder, Colorado

VALERIE M. RODRÍGUEZ CASTRO

Pre-College Internship Program, NCAR, Boulder, Colorado, and Department of Mechanical Engineering, University of Puerto Rico, Mayagüez, Puerto Rico

PAOLA S. ESTEBAN PÉREZ[a]

Pre-College Internship Program, NCAR, Boulder, Colorado, and Colegio San José, Cajicá, Colombia

ABSTRACT

Wind profiling radars are usually not calibrated with respect to reflectivity because such calibrations are both unnecessary for good wind measurements and costly. However, reflectivity from calibrated profilers can reveal many atmospheric attributes beyond winds. Establishing ways to calibrate these radars even after they have been taken out of service would expand the utility of archived profiler data. We have calibrated one operating mode of a 915-MHz profiler deployed at Manus, Papua New Guinea (1992–2001), using two methods. The first method adjusts a radar parameter until the profiler's estimate of rainfall during stratiform events closely matches surface observations. The second adjusts the parameter so that mean brightband heights observed by the profiler (July 1992–August 1994) match the mean brightband reflectivities over the profiler as observed by the TRMM Precipitation Radar (January 1998–July 2001). The results differ by about 5% and yield very similar precipitation errors during tested stratiform events. One or both of these methods could be used on many other wind profilers, whether they have been decommissioned or are currently operational. Data from such calibrated profilers will enable research employing the equivalent reflectivity factor observed by profilers to be compared with that from other radars, and will also enable turbulent studies with C_n^2.

1. Introduction

Atmospheric conditions over the tropical Pacific Ocean affect not only the local landmasses and ocean, but also remote regions of the globe via teleconnections associated with such phenomena as ENSO and the Madden–Julian oscillation. To mitigate what have historically been sparse atmospheric observations in this region the NOAA Aeronomy Laboratory deployed a network of wind-profiling radars (Fig. 1), first as part of TOGA COARE (Parsons et al. 1994) and then under the auspices of the NOAA Climate Program Office (McPhaden et al. 1998).

The profilers in the Trans-Pacific Profiler Network (TPPN), which also included the Australian Bureau of Meteorology's systems at Darwin, Australia, served as components of field campaigns such as COARE and the Maritime Continent Thunderstorm Experiment (MCTEX; Keenan et al. 2000). All the profilers except those at Darwin were decommissioned after about a decade of operation.

TPPN data have been used in many short- and long-term regional studies of dynamics and precipitation (e.g., Williams et al. 1995; Schafer et al. 2001; Hartten and Datulayta 2004; Zhang et al. 2004), sometimes after being merged with data from other platforms (Ciesielski et al. 1997; Hartten 1998). However the profiling radar community has long desired to extract more atmospheric information from profilers than merely winds. Possibilities have included turbulence (Gossard 1977; Chadwick and Moran 1980; Gossard et al. 1998;

---

[a] Current affiliation: Universidad de La Sabana, Chía, Colombia.

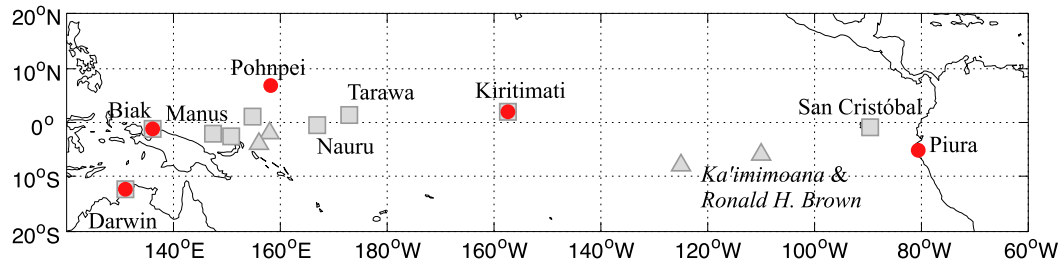*Corresponding author*: Leslie M. Hartten, leslie.m.hartten@noaa.gov

FIG. 1. The TPPN deployed by the NOAA Aeronomy Laboratory and partners during the period 1985–2005. Red circles indicate 50-MHz profilers; gray squares (triangles) indicate 915-MHz profilers on land (ships). Shown but not labeled are the 915-MHz systems deployed in the west Pacific for only 4–6 months during TOGA COARE at Kavieng, Kapingamarangi, R/V *Kexue*, and R/V *Shiyan*. The positions shown for R/Vs *Ka'imimoana* and *Ronald H. Brown* are meant only as indicators of their presence servicing TAO buoys throughout the tropical Pacific.

McCaffrey et al. 2017), precipitation (Rogers et al. 1993; Réchou et al. 2014), drop size distributions (Wakasugi et al. 1986), temperature (Matuura et al. 1986; Angevine et al. 1994; Görsdorf and Lehmann 2000), and humidity (Stankov et al. 1996; Bianco et al. 2005). Some of these measurements require or are enhanced by a *calibrated* profiler, because that enables the calculation of C_n^2, the structure function of the index of refraction, and Z_e, the equivalent reflectivity factor reported by precipitation radars.

Calibration is the process of establishing how to convert relative measured quantities into absolute quantities. Wind profiling radars are calibrated for wind; a $10\,\mathrm{m\,s^{-1}}$ wind reported by one profiler is the same speed as a $10\,\mathrm{m\,s^{-1}}$ wind reported by another, within the error bars associated with the accuracy of each profiler. However, wind profilers are typically not calibrated in terms of the reflectivity measurements because such calibration is difficult, often expensive, and not required for wind measurements. Thus while the signal-to-noise ratio (SNR) measured by profilers can easily be converted into a *relative* reflectivity, the reflectivities calculated from SNR measured in the same conditions by two wind profilers are not expected to be the same; they are not *absolute* or calibrated reflectivities.

There are two basic ways to calibrate a radar. The first involves working with a version of the radar equation, such as

$$P_r(r_0) = \iiint \eta(r) \frac{C_0 f^4(\theta,\phi)|W(r_0,r)|^2}{l(r)^2 r^4} r^2 \, dr \sin\theta \, d\theta \, d\phi \tag{1}$$

(Johnston et al. 2002; after Doviak and Zrnić 1993). The $P_r(r_0)$ is the power received at range r_0; $\eta(r_0)$ is the volume reflectivity and $l(r_0)$ the signal attenuation over the range; $f(\theta, \phi)$ is the antenna's spatial response, dependent on azimuth angle θ and elevation angle ϕ; $W(r_0, r)$ is the range-weighting function; and C_0 is a constant specific to the particular radar being calibrated. This

formulation assumes that atmospheric attenuation can be ignored, since the wavelengths used have small absorption values ($<0.01\,\mathrm{dB\,km^{-1}}$) and small ranges ($<10\,\mathrm{km}$) (Ulaby et al. 1981). The direct method of calibration is to evaluate each term in the radar equation so that $P_r(r_0)$ is determined in absolute power units (watts or the equivalent). This method of calibration requires careful measurement of the transmitted power, all antenna characteristics, transmission line losses, receiver losses, receiver filter functions, and signal processing factors. Accurate and precise measurements of these quantities, especially those concerning the antenna, are difficult and expensive to perform.

The second way to calibrate a radar involves the use of a transfer standard (i.e., comparison against another known measurement). This comparison can occur at the level of a directly measured quantity, such as power returned from a known target, or of a derived one such as rainfall. This second method is the only option for a radar that has been decommissioned, and may also be preferred for extant radars because it can result in a better calibration as well as saving the time and monetary costs associated with a direct calibration.

Since 915-MHz radars are sensitive to both clear-air (Bragg) scattering and hydrometeor (Rayleigh) scattering, precipitation events offer a good opportunity to calibrate these radars after they have been deployed, even after they have been removed from the field. Hartten and Johnston (2014), working with observations collected aboard the NOAA ship *Ronald H. Brown* in the equatorial east Pacific, used shipboard tipping-bucket rainfall measurements during a stratiform rain episode to calibrate the ship's 915-MHz wind profiler. Johnston et al. (2017) used the same technique to calibrate a Colorado-based frequency-modulated continuous-wave (FM-CW) 2835-MHz radar with separate transmit and receive antennas.

In the western equatorial Pacific, where most of the long-term deployments of tropical profilers occurred,

taking advantage of the frequent stratiform rain events is a good strategy. Stratiform rain is characterized by a distinctive radar signature called the bright band, a layer of strongly enhanced reflectivity where falling snow is beginning to melt (White et al. 2002). The bright band is very visible to 915- and 2835-MHz profiling radars, a key factor in the aforementioned successful calibrations. It is also visible to the precipitation radars on the TRMM (Kummerow et al. 1998) and GPM (Hou et al. 2014) satellites. Brightband height and reflectivity are standard products from those satellites. Could they be used to calibrate profilers?

Here we document our efforts to use two different methods to calibrate the 915-MHz profiler deployed at Manus, Papua New Guinea. Our goal was not to obtain perfect profiler precipitation estimates, but to evaluate two different calibration methods for no-longer-extant profilers. Both methods involve a transfer standard; one utilizes rainfall from a tipping-bucket rain gauge located near the profiler, while the other involves long-term statistics of brightband reflectivities from the TRMM Precipitation Radar. The methods were implemented independently, initially as student research projects conducted during the summer of 2014. The two calibrations were then compared with each other and verified using additional stratiform rain events before a final calibration was determined.

2. Radars and precipitation

Stratiform rain is characterized by frozen particles falling from high in the atmosphere that produce enhanced reflectivity as they melt. The resulting bright band can be used to distinguish stratiform rain from other precipitation. The bright band occurs just below the 0°C level, which in the tropics is typically 4–6 km above the surface. Both of our calibration methods take advantage of the bright band, although in different ways.

Wind profilers deal primarily with reflections from volume scattering, which are analyzed at each sample range to give an average power spectrum of the returned signal. The power spectrum at each range is analyzed to get SNR, radial velocity, and spectral width, which are used to describe the state of the atmosphere.

To test the two calibration methods, we use data from the 915-MHz wind profiler that was located in the Manus province of Papua New Guinea. It was deployed in July 1992 at Momote Airport (2.06°S, 147.42°E) on Los Negros Island, which lies just east of the province's main island of Manus (Fig. 2a), and ran more-or-less continuously until October 2001. We chose this profiler both for its extensive data record and because it was one of the most reliable tropical profilers deployed by NOAA.
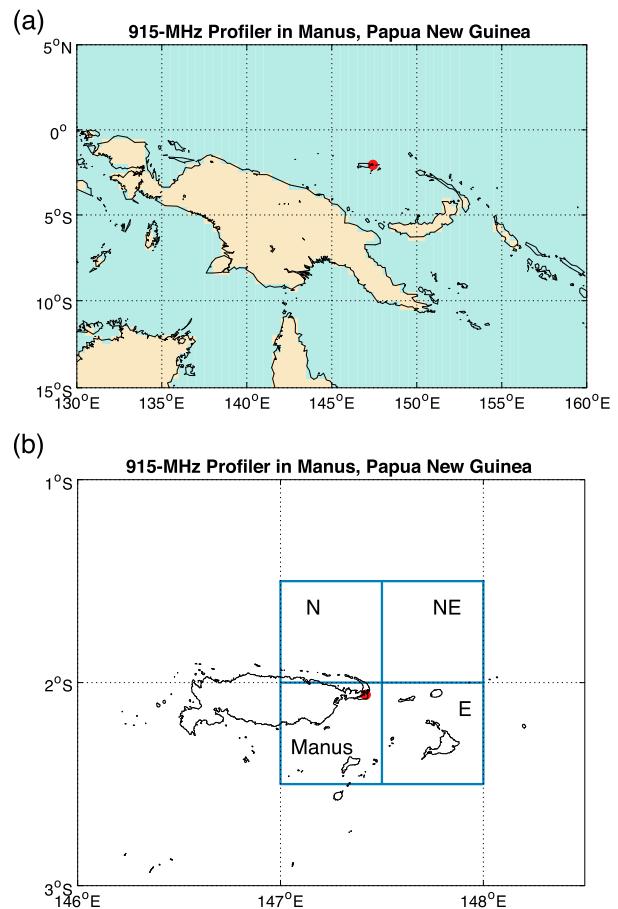

FIG. 2. (a) Map of the island of Papua New Guinea and environs, with the location of Momote Airport indicated by a red circle. Shading is based on the 0.5° × 0.5° boxes classified as land (tan) or ocean (blue) in the TRMM dataset. (b) Map of Manus Island and environs, including Los Negros Island just to its east where Momote Airport is located (red circle). The TRMM grid box containing the Manus profiler, as well as the boxes to its north, northeast, and east, is outlined in blue; all are classified as ocean in the TRMM dataset.

This was a 3-beam phased-array system; the dwell time in each beam was nominally 38 s. It operated in two interleaved modes: a "low mode" with 105-m vertical spacing up to 5.2 km, and a "high mode" with 255-m vertical spacing up to 12.5 km. More details can be found in Carter et al. (1995) and Gutzler and Hartten (1995). We exclusively used data from the vertical beam of the low mode.[1] Because of the scanning strategy employed, these data occur approximately every 3.8 min. In addition to the

---

[1] Raw spectral data as well as postprocessed winds from the TPPN profilers are archived at the NOAA Earth System Research Laboratory's Physical Sciences Division (see https://www.esrl.noaa.gov/psd/data/).

analyzed profiler data (SNR, velocity, spectral width, and noise level), the average power spectra from all ranges and times were recorded. These power spectra provide the dataset used for calibration of this radar.

Collocated with this radar was a surface meteorological system that recorded 1-min time series including rain accumulation. Rain was measured by a TE525 tipping-bucket rain gauge with tip increment of 0.254 mm (Miller and Riddle 1994). Its reported accuracy was $\pm 1\%$ for rainfall rates up to $1\,\mathrm{in.\,h^{-1}}$ and $+0\%$, -3% from 1 to $2\,\mathrm{in.\,h^{-1}}$ (Campbell Scientific 2004). The gauge was placed in a fairly open location near the profiler and other surface instruments but without any special screening, and in our experience the surface data during the later years of the deployment was not as good as during the earlier periods. This rain accumulation provides the transfer standard for one of the calibrations.

The other calibration used data from the TRMM satellite as the transfer standard. The TRMM satellite, launched on 27 November 1997, was designed to provide consistent measurements of precipitation throughout the tropics, with high resolution in both time and space (Kummerow et al. 2000). It was initially placed in an orbit that ranged from 35°S to 35°N at 350 km; in August 2001 this was boosted to 402.5 km. Its orbit was such that it passed directly over any given location daily, with the time of day repeating every 42 days. In summer 2014, with its fuel nearly spent, it began to slowly descend and instruments were turned off in April 2015.

The TRMM satellite carried a calibrated Ku (13.8 GHz) Precipitation Radar (PR) with 250-m vertical resolution. The radar's original nadir footprint of 4.3 km increased to 5.0 km after the boost. An evolving set of algorithms have been used to process its data. Of particular relevance for this work is the TRMM 2A23 algorithm, which classifies radar retrievals into different precipitation types. Version 6 was released in 2004 (Awaka et al. 2009) and version 7 in 2011 (Funk et al. 2013). We use version 7 monthly mean values of brightband heights and reflectivities, which have been released as part of the 3A25 dataset. These are available on a $0.5° \times 0.5°$ grid and come with an associated land/ocean mask. All of the grid points near Manus are classed as "ocean" points (Fig. 2a).

3. Calibration against surface measurements

Our first calibration involves comparing the rainfall estimated from profiler reflectivity during selected stratiform rain events with the rainfall measured at the surface by a tipping-bucket rain gauge. We focus on 1 November 1992–28 February 1993, the COARE intensive observing period (IOP), since it is a well-studied

period with good quality data and the rain and profiler datasets were readily available to us.

We used custom software (PDAprecipAll) to estimate rain from profiler reflectivity. This software, whose algorithms and effects are described in more detail in appendix A, recomputes the SNR using the power spectra from the low-mode vertical antenna dwells, making corrections for coherent-averaging filter effects (Gage and Balsley 1978) and noise fluctuations. Using a simplified version of the radar equation, PDAprecipAll determines the radar reflectivity factor Z_e (dBZ) at each range r (m):

$$10^{Z_e(r)/10} = \frac{\mathrm{PRC}}{\mathrm{NPW}^2 \mathrm{NCI}} r^2 10^{\mathrm{SNR}(r)/10}. \qquad (2)$$

NPW is the transmitted pulse length in nanoseconds, NCI is the number of coherent averages used in the data processing, SNR is in decibels (dB), and all other parameters are lumped into the profiler radar constant PRC ($10^{-18}\,\mathrm{mm^6\,m^{-5}\,s^2}$). PDAprecipAll classifies the resulting reflectivities; those with SNRs smaller than the Riddle threshold (Riddle et al. 2012) are classified as "no signal detected." It then uses cluster analysis results to categorize the remainder as precipitation or nonprecipitation (Williams et al. 2000). The software also computes four different rain rates for each dwell using Z–R relationships for convective, stratiform, and warm rain, and snow (Zhang et al. 2011).[2] For stratiform rain, the Marshall–Palmer Z–R relationship $Z = 200R^{1.6}$ (Marshall et al. 1955; Zhang et al. 2011) is used, where Z is the reflectivity in linear units ($\mathrm{mm^6\,m^{-3}}$) and R is the rain rate ($\mathrm{mm\,h^{-1}}$). If an echo is classified as precipitation, the rain rate is multiplied by the duration from the start of the current record to the start of the next observation to get the accumulation for the observation period. This accumulation is then added to the total accumulation for the analysis period. Since our initial reflectivity is not well calibrated, our estimation is an iterative process.

We wanted to calibrate using one or more long-lived periods of stratiform rain that produced large accumulations on the ground. This increases the likelihood that the many possible sources of small errors (e.g., evaporation in the air, spatial and temporal mismatches, horizontal advection) average out, thereby increasing the robustness of our result. During the 4-month IOP, there were 10 days on which the following criteria were met: a complete set of observations from both platforms, uncategorized daily rainfall $\geq$ 10 mm, and profiler-detected precipitation

---

[2] The National Mosaic and Multi-Sensor Quantitative Precipitation Estimation (QPE) (NMQ) system described in Zhang et al. (2011) also includes a Z–R relationship for hail.

TABLE 1. On the left are the four rain events used to calibrate the profiler and verify the calibrations, together with the rain gauge accumulation C_{gauge} and the best profiler radar constant (PRC) for each event. On the right are average profiler-based accumulations $\overline{C}_{PRC}$ and associated performance measures calculated with three PRCs: $PRC_{surface}$ (= 115.198), obtained by averaging PRCs obtained by using the rainfall during the primary events as the transfer standard; $PRC_{satellite}$ (= 121.036), obtained by using July 1992–August 1994 TRMM brightband reflectivities as the transfer standard; and PRC_{final} (= 118.117), their average. The $\overline{C}_{PRC}$ and the range are from profiler-based precipitation estimates at range gates 4–8, while the error is calculated as $(\overline{C}_{PRC} - C_{gauge})/C_{gauge} \times 100$.

Event	Gauge accumulation (mm)	Best PRC for event	Profiler accumulation (mm) using $PRC_{surface}$			Profiler accumulation (mm) using $PRC_{satellite}$			Profiler accumulation (mm) using PRC_{final}		
			Mean	Range	Error	Mean	Range	Error	Mean	Range	Error
Primary events											
1216–1646 UTC 14 Dec 1992	13.462	108.914	13.942	0.254	+3.57%	14.380	0.262	+6.82%	14.162	0.258	+5.20%
0110–0635 UTC 28 Jan 1993	14.224	121.483	13.779	0.152	−3.13%	14.211	0.157	−0.09%	13.996	0.155	−1.60%
Reserve events											
0529–0700 UTC 11 Dec 1992	5.588	167.911	4.416	0.494	−20.97%	4.522	0.510	−19.08%	4.485	0.502	−19.74%
1042–1310 UTC 27 Jan 1993	8.636	68.242	11.979	1.527	+38.71%	12.355	1.575	+43.06%	12.168	1.551	+40.90%

over a total of at least 5 h. The amount and duration criteria were designed to help us winnow out days that might have long-lived and relatively heavy stratiform rain. We examined the character of the reflectivity and the bright band during these 10 days to identify long-lived stratiform events, then selected two primary events and two reserve events (Table 1). None of the events both produced ≥10 mm rain and lasted ≥5 h, and two did neither; however, we judged them the best available for our purposes.

The first primary event, on 14 December 1992, featured stratiform rain from 1216 to 1646 UTC[3] embedded within a longer period of precipitation (Fig. 3a), during which time the gauge recorded 13.462 mm of rain. During the second primary event, on 28 January 1993, the uncalibrated profiler reflectivity showed a broken bright band (Fig. 3b) and the gauge measured 14.224 mm of rain from 0110 to 0635 UTC. The bright bands during the reserve events, on 11 December 1992 and 27 January 1993, were much shorter lived and produced much less rain, with the stratiform rain on 11 December being preceded by a period of heavy convective rain.

We started the calibration with PRC = 65, a value that had previously been established for a similar radar. We compared the gauge accumulations during the primary events with the estimated profiler accumulations derived by PDAprecipAll using this PRC. The time limits during this initial pass, which were established visually from plots of uncalibrated reflectivity similar to those shown in Fig. 3, differed by 5–55 min from the times

listed in Table 1. We initially looked only at the lowest eight range gates (altitudes) of the profiler, to balance the risk of evaporation or advection of raindrops detected at higher altitudes in a larger volume against the risk of nonlinear radar response in the lowest gates. The plots of accumulated rainfall as a function of time (Fig. 4) clearly showed that the first two gates needed to be excluded, as their estimated accumulations were distinctly less than those from the higher gates. This was not a surprise; these lower two range gates can provide good velocity measurements, but are subject to saturation, recovery issues, and gradients in the radar response within the sampled volume,[4] all of which make reflectivity measurements difficult (Johnston et al. 2002). These results were otherwise encouraging; on both days the accumulations from gates 3 to 8 were tightly clustered and evolved similarly to the gauge accumulation.

The results in Fig. 4 indicated that we needed a larger PRC value; we tried again with PRC = 85 and then PRC = 110. As we iterated, we also refined our technique. We removed the third range gate from the evaluation since it also showed nonlinearity in its response,

---

[3] Unless otherwise noted, rainfall times will be based on the start and end of the stratiform rain recorded by the rain gauge, where identification of "stratiform" is based on profiler data.

[4] One of the assumptions deeply buried in the radar equation typically used for profiling radars is that the range is much larger than the pulse width (i.e., than the length of the volume). One effect of this assumption is our ability to assign the volume reflectivity to the center of the range. However, the radar response within a volume falls off as r^2, so when the range is on the order of the pulse width the contribution to the volume reflectivity by the near-scattering field is considerably larger than that from the far field, and assigning that reflectivity to the centroid is incorrect. See Johnston et al. (2002) for more precise details.
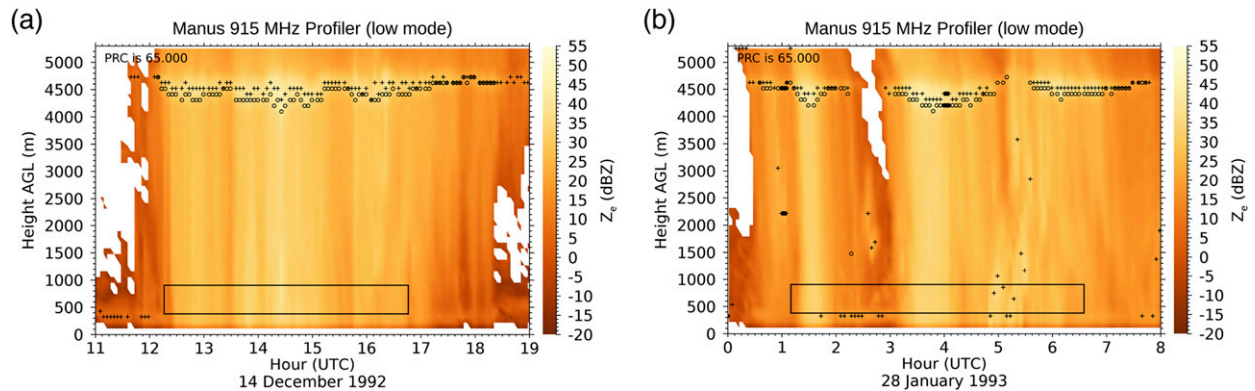
FIG. 3. Initial, poorly calibrated reflectivity (dB) from the Manus profiler's low-mode vertical beam for several hours during the calibration days (a) 14 Dec 1992 and (b) 28 Jan 1993. Circles indicate the brightband heights, which were determined by the BBH algorithm (White et al. 2002), while pluses identify the peak reflectivity in each profile as determined by PDAprecipAll (see appendix A). The heights and times of the data used for the calibration are indicated by a box.

although not as dramatically as the lowest two ranges. We examined the PDAprecipAll results (PRC = 110) from each scan during a 2-h period centered on the beginning and ending time of the profiler time series, comparing the precipitation classification and vertical velocities in range gates 4–8 with the subsequent rain gauge data, thereby refining the start and finish times of the stratiform rain to the values in Table 1.

After this exploratory work, we started over. We reran PDAprecipAll with PRC = 65, using our final start and end times for the two calibration cases. This yielded an average accumulation over gates 4–8 of 9.75 mm for the 14 December 1992 event and 9.622 mm for the 28 January 1993 event. (Unless otherwise noted, profiler accumulations will henceforth refer to the average of the accumulations in gates 4–8.) We used (2) and the Marshall–Palmer relationship to estimate a new PRC via

$$PRC_{new} = PRC_{old} \left(\frac{C_{gauge}}{C_{profiler}} \right)^{1.6} \qquad (3)$$

for each case: 108.914 for 14 December 1992 and 121.483 for 28 January 1993. The resulting differences between the gauge and the profiler accumulations were $+4.0 \times 10^{-5}$ mm on 14 December 1992 and -0.02 mm on 28 January 1993, so small that we accepted these values as the best PRCs for those events. Since our goal is a single calibration and the 11% difference between the two PRCs is small, we averaged these two event-best PRC values to get a final surface-based PRC of 115.198, hereafter $PRC_{surface}$. Employing $PRC_{surface}$ gives a mean radar accumulation that is $+3.57\%$ (0.480 mm too high) for the 14 December case, and -3.13% (0.445 mm too small) for the 28 January case (Fig. 5 and Table 1). These differences are within the

accuracies specified for operational tipping-bucket rain gauges in the United States (± 0.508 mm, or 4% of hourly total, whichever is larger; National Weather Service 1998).

We chose total accumulation as our calibration standard under the premise that the short-term variability averages out in the accumulation. Figure 5 demonstrates this variability quite well; the radar accumulation and the rain gauge do not follow each other exactly. Many factors can cause this to happen: changes in rain rate between radar observations, variability in the applicability of the chosen Z–R relationship, advection of radar-observed rain away from the rain gauge, or fall time from gate height. These effects are minimized by summing over time. The range of final accumulations at gates 4–8 during each event is also remarkably small, indicating that the processes that could cause small spatial variability were minimal. These factors make these strong events for calibration work.

4. Calibration against satellite measurements

Our second calibration involves matching long-term mean brightband reflectivities measured by the profiler with long-term mean brightband reflectivities from the TRMM PR. For the profiler data, we focused on July 1992 through August 1994,[5] the first two years the

---

[5] Our decision to use this period was in part due to familiarity with the quality of the data during those years and easy access to those data. However it was also driven by logistical considerations. Much of the calibration work was to be done in parallel by precollege summer interns Rodríguez Castro and Esteban Pérez in collaboration with Hartten while Johnston was preparing for and conducting field work in remote locations. Using the same time periods for surface data and for verification profiler data was critical in enabling a rewarding summer research experience.
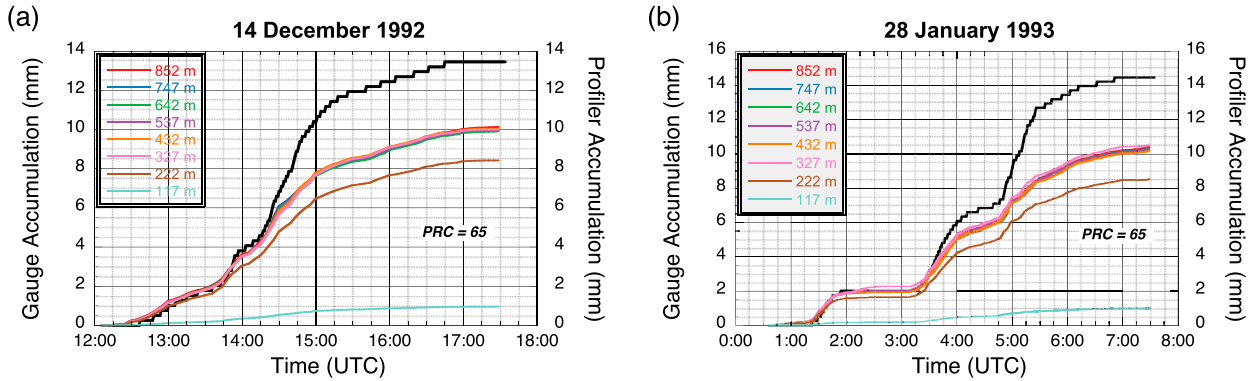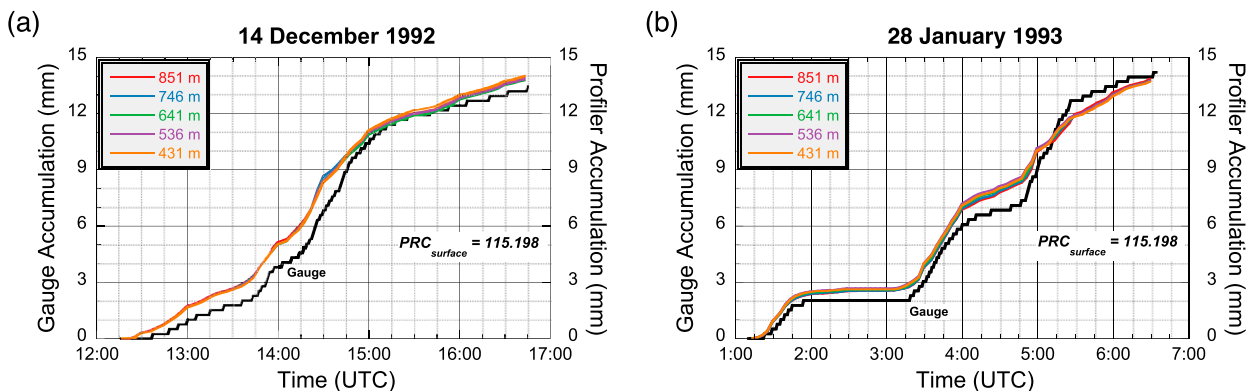
FIG. 4. Comparison of gauge accumulated rainfall (thick black line) and profiler-estimated rainfall for the default PRC = 65 during the primary rain events on (a) 14 Dec 1992 and (b) 28 Jan 1993.

profiler operated, and again on the low mode's vertical beam. We assumed that the bright band would occur at or above 3 km, which amounts to using a very conservative lowest estimate of the freezing level in this location (Johnson et al. 1996), and that PRC = 65 was a good starting point. We then processed the profiler data using two different pieces of software. The first algorithm, MAXR (part of PDAprecipAll; see appendix A), estimates the maximum reflectivity in a profile and identifies its height, for heights above 3 km. The second algorithm, BBH, uses both the reflectivity profile as measured by the real-time software and the velocity values in the profile to determine the height of the bright band; it is very good at identifying brightband heights (White et al. 2002). All reflectivity statistics (from both the profiler and the TRMM data) were computed in log space (dBZ).

We combined the good reflectivity values from MAXR with the very good brightband heights from BBH as follows. BBH identified 13 397 vertical profiles containing a bright band. We extracted, from the output of MAXR, the height of the maximum reflectivity in each of those

profiles and its reflectivity. The distributions of the height of the maximum reflectivity above 3 km in all profiles with a bright band (Fig. 6a) and the height of the bright band (Fig. 6b) are quite similar; the median height is about 4500 m and lies within a broad peak between 4 and 5 km, although the maximum reflectivities skew a little higher than the median while the bright bands skew a little lower. The distribution of maximum reflectivities has secondary maxima at 3 km (our cutoff) and 5200 m (the highest range gate). The former can occur in the absence of a bright band if reflectivity is decreasing with height across the 3-km level. However, when viewed as timed pairs, the heights from MAXR are usually one or two range gates higher than those from BBH (Fig. 6c). We decided to work with only those profiles for which the maximum reflectivity occurred within one range gate (±105 m) of the brightband height. We describe the bright bands observed in those 10 798 profiles in terms of heights from BBH and maximum reflectivities from MAXR. The long-term mean estimated (uncalibrated) reflectivity of these bright bands was 27.4 dB.
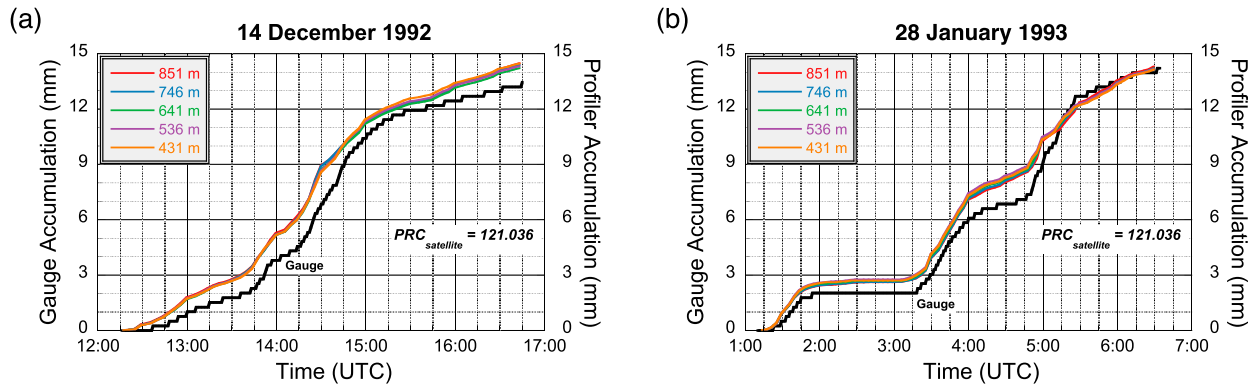

FIG. 5. Comparison of gauge accumulated rainfall (thick black line) and profiler-estimated rainfall for the final surface-based PRC, PRC$_{surface}$ = 115.198, during the primary rain events on (a) 14 Dec 1992 and (b) 28 Jan 1993.

(a)

(b)

(c)
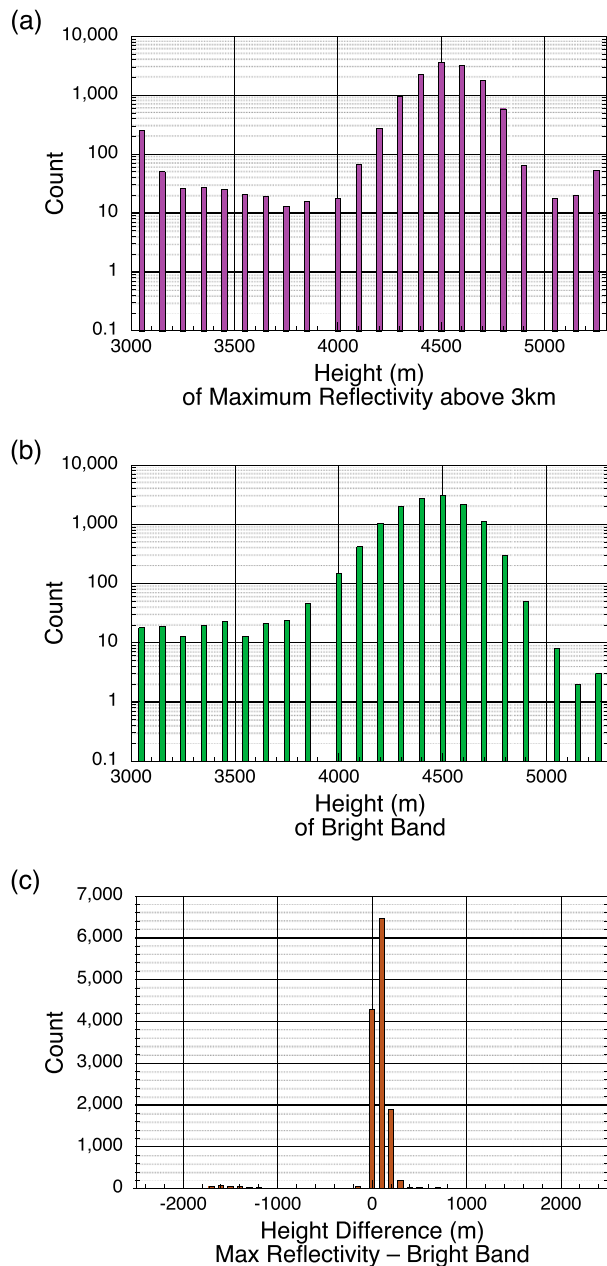
FIG. 6. Distributions of (a) the height of the maximum reflectivity above 3 km, determined by the MAXR algorithm, (b) the height of the bright band identified by the BBH algorithm, and (c) the difference between time-matched pairs of the two. All data are from vertical scans by the Manus profiler's low mode, July 1992–August 1994, during which a bright band was detected. The mean and median heights associated with the data plotted in (a) are 4514 and 4527 m, respectively, while the mean and median heights associated with the data plotted in (b) are 4459 and 4527 m, respectively.

There is no temporal overlap between the TRMM satellite and the early years of the Manus profiler, which is one reason we are relying on long-term statistics for this calibration method. Since matching times was not possible, we decided to work with the preboost (January 1998–July 2001) TRMM data, which had a slightly smaller footprint that the later data. We recognize that signals related to El Niño–Southern Oscillation permeate the tropical west Pacific's ocean/atmosphere system, including the freezing-level height (Bradley et al. 2009). However, we are unaware of a physical mechanism that would cause brightband reflectivities to be a function of ENSO. Our brief analysis of brightband heights and reflectivities near Manus (appendix B) indicates that variations in ENSO's phase during the different time periods appear unlikely to have an adverse effect on the calibration.

For each month we spatially averaged the mean brightband heights and reflectivities at each of the four TRMM grid points closest to Manus (cf. Fig. 2), as well as over their combined area. Each time series exhibits considerable month-to-month variability including months with no brightband observations (Fig. 7). The Manus grid point had more months with observed bright bands (35) than did the others (28–31), but not as many as the combined area (38). The total number of observed bright bands was slightly higher northeast of Manus (2040) than at Manus (2002).

In light of the large variation between grid boxes and the high number of observed bright bands and months with bright bands in the Manus grid box, we decided to use the Manus grid point alone to obtain a long-term mean TRMM brightband reflectivity. The median of the monthly averaged brightband heights is 4512 m, which is within the peak of both distributions of profiler brightband height in Fig. 6 and increases our confidence that the profiler and the satellite are looking at similar bright bands. The preboost long-term mean brightband height was 4476 m and the mean reflectivity was 30.10 dBZ. Both long-term means were calculated by weighting monthly values by the number of bright bands observed in that month, then dividing the sum of the weighted values by the total number of observed bright bands. The number of profiles per month is shown in Fig. 7. The difference between the TRMM and the profiler brightband reflectivities is 2.70 dB, and (2) tells us that reflectivity is proportional to PRC. Increasing the profiler reflectivity by 2.70 dB so that it matches the TRMM reflectivity requires a PRC value of 121.036, hereafter called PRC$_{satellite}$. This satellite-derived PRC is 5% larger than the surface-determined PRC$_{surface}$.

5. Validation, error analysis, and final equations for Z_e and C_n^2

We have used two fundamentally different techniques to determine a calibration of the Manus profiler.
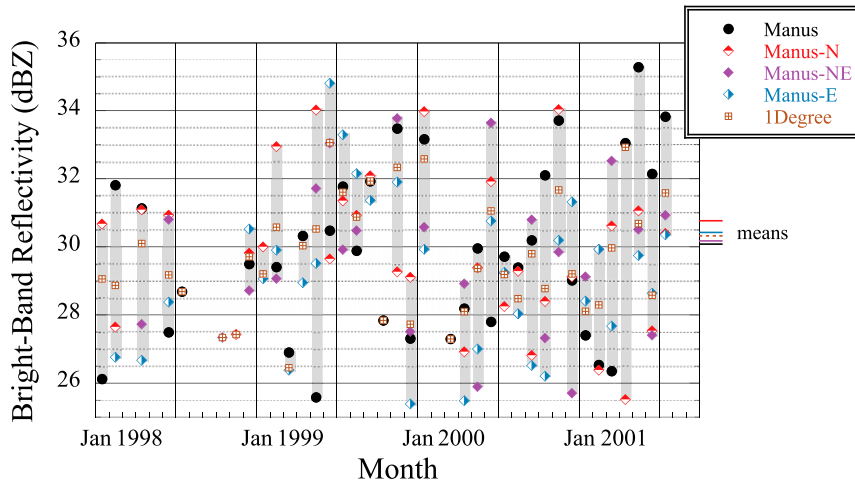
FIG. 7. Monthly TRMM brightband reflectivities (2A23 algorithm, version 7, released as part of the 3A25 dataset) at the grid points nearest Manus (solid black circle), to its north (red diamond), northeast (purple diamond), and east (blue diamond), as well as averaged over those grid points (brown square). Gray shading indicates the range of reflectivities in each month for which more than 1 grid point had brightband data. The January 1998–July 2001 mean reflectivities for each of the time series are indicated by short horizontal lines along the right axis (solid for individual grid points, dashed for averaged over all).

The methods give calibration constants that differ by 5%. This small difference increases our confidence in our ability to calibrate the Manus radar. Before determining a final calibration factor, we validated the surface-based $PRC_{surface}$ on two reserve events and the satellite-based $PRC_{satellite}$ against all four primary and reserve events and then performed some error analysis.

a. Validation of $PRC_{surface}$ and $PRC_{satellite}$ against independent events

Estimating rainfall from profiler data during the primary cases using $PRC_{satellite}$ results in accumulations that are +6.8% (0.918 mm high) for the 14 December 1992 case and −0.1% (0.013 mm low) for the 28 January 1993 case (Fig. 8; Table 1). While $PRC_{satellite}$ gave twice as big an overaccumulation as $PRC_{surface}$ on 14 December and a very small underaccumulation on 28 January, these profiler accumulations are still very close to the gauge amounts. During both events the range of accumulations in the five profiler gates is about 0.2 mm (±0.05 mm; Table 1) no matter which PRC is used.

Turning to the reserve cases, both $PRC_{surface}$ (= 115.198) and $PRC_{satellite}$ (= 121.036) yield profiler rain accumulations during the 11 December 1992 event that are about 20% (1 mm) less than the gauge accumulation (Table 1), a difference that approaches the accuracy of the gauge. The accumulation in gates 4–8 based on $PRC_{surface}$, together with the gauge accumulation, are shown in Fig. 9a. Throughout the event, the profiler accumulation lags the gauge accumulation, with the

largest discrepancy occurring during the period of rapid gauge accumulation from 0538 to 0544 UTC. The profiler estimates are not as tightly clustered as they were in the calibration cases (cf. Figs. 5, 8 and Table 1) but diverge as time progresses, especially from about 0600 UTC onward. Their spread is not necessarily a surprise since precipitation observed at greater distances from the surface has more time to evaporate or to advect away from the surface gauge. What is surprising is that the highest accumulation comes from the lowest gate rather than the highest. The manner in which the profiler accumulation lags the gauge accumulation, coupled with higher profiler accumulations at lower gates, strongly suggests that heavier rain is being horizontally advected toward the site and that during this case the effect increases closer to the ground, although we have not examined any ancillary data to try to confirm or refute this idea.

During the 27 January 1993 reserve case both $PRC_{surface}$ and $PRC_{satellite}$ yield profiler accumulations of rain that are about 40% (3.5 mm) more than the gauge accumulation (Table 1); Fig. 9b shows the accumulation in gates 4–8 based on $PRC_{surface}$. The profiler accumulation led the gauge accumulation throughout the event, with the difference increasing fairly steadily from 1130 UTC onward. The range of the final individual gate estimates is about three times that in the 11 December verification case (Table 1), but the estimates increase with the height of the range gate.

We chose the primary events because their long duration and relatively large rainfall increased the chances

FIG. 8. Comparison of gauge accumulated rainfall (thick black line) and profiler-estimated rainfall for the final satellite-based PRC, $PRC_{satellite} = 121.036$, during the primary rain events on (a) 14 Dec 1992 and (b) 28 Jan 1993.

that small errors would average out and because their strong brightband reflectivities increased the chances that they were truly stratiform rain and thus well modeled by the Marshall–Palmer Z–R relationship. The calibration and verification process have shown that profiler estimates of accumulated rain during these cases are very consistent with height (with a range of 1%–2% of the gate-average accumulation) and evolve very similarly to the surface observations. In contrast, the reserve events involved less total rainfall and the profiler estimates of accumulated rain during the reserve events are much less consistent with height (range of 11%–13% of the average). The estimates evolve differently than the surface observations, and one even diverges differently than all the other cases. Changing the PRC would not change those facts, as different PRCs will only tilt the accumulations curves up or down. Since these reserve events occur one to three days before the primary events, radar changes are unlikely and it appears that the spread in profiler accumulations is related to meteorology rather than instrumentation.

Overall, the errors in profiler-based rain estimates using either $PRC_{surface}$ or $PRC_{satellite}$ are of similar small magnitude. Given our data's limitations, especially the ~3.8-min gap between 38-s observations of the rain (which forces us to assume the rain rate is constant between observations), we are pleased with the great agreement between the surface and the gates in this calibration.

b. Effect of PRC choice

We can use $PRC_{surface}$ and the associated profiler accumulation from the reserve events in one final iteration of (3) to calculate the best PRC for those two events (Table 1). Combined with the results from section 3, this yields "event best" PRCs ranging from 68.242 to 167.911. The largest and the smallest PRCs come from the reserve events, which were shorter lived and involved smaller rain accumulations than the primary events. It is also possible that the rainfall during them not uniformly stratiform in nature, so that the Marshall–Palmer Z–R relationship was not a good fit,
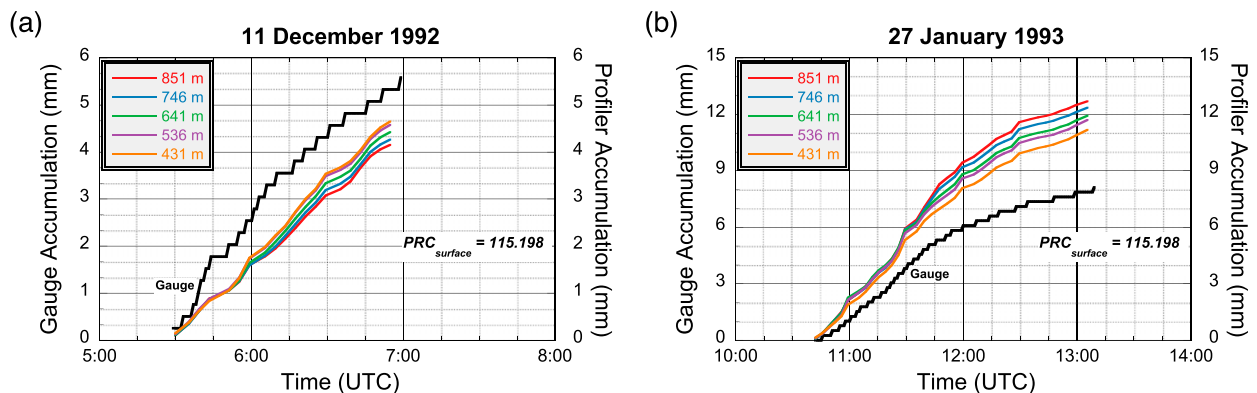
FIG. 9. Comparison of gauge accumulated rainfall (thick black line) and profiler-estimated rainfall for the final surface-based PRC, $PRC_{surface} = 115.198$, during the reserve rain events on (a) 11 Dec 1992 and (b) 27 Jan 1993.

or it could be that the rainfall was evaporating or horizontally inhomogeneous, so that the assumption that rain in the vertical beam hit the gauge was not a good one. Regardless, the average of all four event-best PRCs is 116.637, larger that $PRC_{surface}$ and smaller than $PRC_{satellite}$.

We trust $PRC_{surface}$ more than any individual surface-based PRC or any other average of surface-based PRCs because the two primary events are longer, have more rain, and yield more similar results than the reserve events. The values of $PRC_{surface}$ and $PRC_{satellite}$ are very close to each other and yield errors of similar magnitude when estimating precipitation during the calibration and verification events. Since we have no particular evidence on which to prefer one over the other, we will henceforth work with the average of $PRC_{surface}$ and $PRC_{satellite}$, denoted PRC_{final}, which is 118.117.

The Manus radar and rain gauge are no longer available, which makes it difficult to assess instrument accuracies. However the sensitivity to changes in measurements can be evaluated by using (3) to estimate PRC values for hypothetical changes in rain accumulation. If the rain gauge underestimated the accumulation by 10%, the new PRC would be 137.576 $[PRC_{+10\%} = PRC_{final}(1.1)^{1.6}]$. Similarly, a 10% overestimation by the rain gauge would change the PRC from 118.837 to 99.793 $[PRC_{-10\%} = PRC_{final}(0.9)^{1.6}]$. Since (2) shows that Z and PRC are proportional to each other, the $\pm10\%$ changes in rain accumulation correspond to ±0.7 dB changes in reflectivity.

c. Final calibration equations

Having decided to use PRC_{final} as the value for calibrating the low mode of the Manus profiler, we can calculate the accumulations estimated by the now-calibrated radar during each event one last time (Table 1). The deviation of these results from the gauge estimates is very comparable to the results using either $PRC_{surface}$ or $PRC_{satellite}$, with event-to-event variability yielding both over- and underestimates that are smallest during the calibration cases.

Using (2) with our radar parameters, the equivalent reflectivity factor Z_e for the radar's low mode can be easily written as

$$Z_e(r) = 10 \log\left(\frac{PRC_{final}}{NPW^2 NCI}r^2 10^{SNR(r)/10}\right)$$
$$= SNR(r) + 20 \log(r) - 57.940, \quad (4)$$

where Z_e and SNR are in decibels. This calibrated reflectivity is directly comparable to the reflectivity observed by any other calibrated radar, provided both radars are illuminating something that both are sensitive to (e.g., precipitation). The calibrated profiler reflectivity during and immediately surrounding our four stratiform rain events is plotted in Fig. 10.

That same equivalent reflectivity factor is shown in Fig. 11 for the entirety of 27 January 1993. Bright bands occurred multiple times during this day, at heights ranging from 4100 to 4600 m. Maximum reflectivities were not always coincident with bright bands, and a bright band aloft did not always lead to strong precipitation near the surface. There was clearly nonstratiform precipitation as well, for example, from 0900 to 1000 UTC, with Z_e = 30–42 dBZ at range gate 4, and around 1700 UTC, with $Z_e \geq 40$ dBZ at range gate 4. The plot also reveals persistent maximum reflectivities at 327 m, the third range gate, most noticeably from 0200 to 0630 UTC. These are probably not atmospheric echoes. Johnston et al. (2002) showed that volume reflectivity from gates close to the radar can be attributed to an incorrect range, which could account for part of the problem. Careful examination of the third range gate might reveal a way that the spectra could be converted to calibrated reflectivities by using a different value of the profiler radar constant PRC.

When it is not precipitating, the Bragg scatter reflectivity measured by the profiler is a function of the index of refraction structure constant C_n^2, which can be related to turbulence in the atmosphere. Using straightforward algebra, the calibrated reflectivity can be expressed in terms of C_n^2 instead of Z_e [see Rogers et al. 1993, their (3) and (4)], again using SNR (dB) and PRC_{final}:

$$\log C_n^2 = -19.1473 + 2\log(r) + 0.1SNR. \quad (5)$$

Reflectivities from two separate days without precipitation, transformed into C_n^2, are shown in Fig. 12. The range of values are reasonable (cf. Nath et al. 2010, their Figs. 1 and 9; Hartten and Johnston 2014, their Fig. 4) although we have not done any special data vetting that might be reasonable for research studies involving C_n^2, for example, examined outliers or investigated possible ground-clutter contamination. During the night of 29 November 1992 (LST), with no solar heating, the boundary layer turbulence decreases, minimizing near local midnight (Fig. 12a). Turbulence intensity increases after sunrise, and again atop what is presumably a deepening convective boundary layer during the afternoon, before again becoming weaker and confined mostly below 1 km at night. The atmosphere evolved somewhat differently on 13 October 1992 (LST). The evolving daytime boundary layer was preceded by low-level turbulence throughout the evening (Fig. 12b). Aloft were as many as three long-lived layers of enhanced reflectivity with varying magnitudes
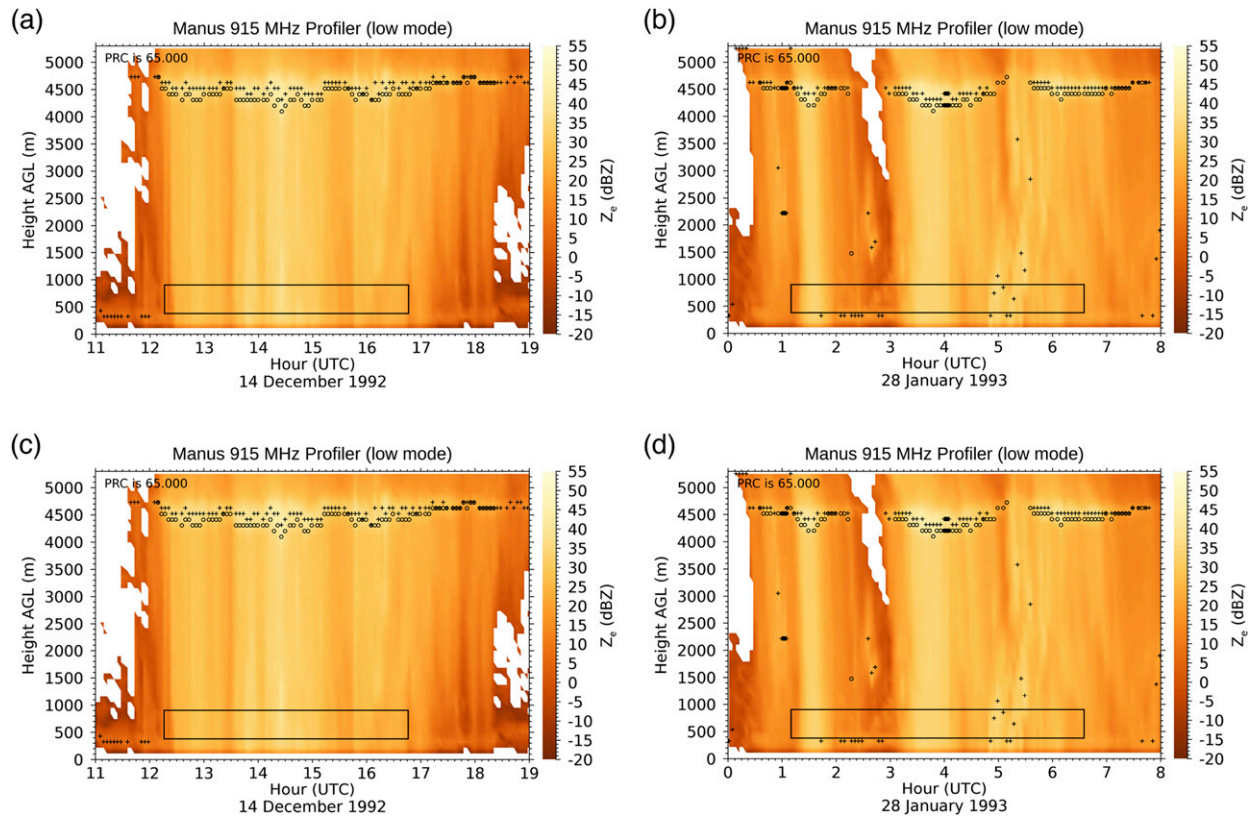
FIG. 10. Equivalent reflectivity factor Z_e during the four stratiform rain events used to calibrate and verify the low mode of the Manus profiling radar. Circles indicate the height of the bright band when it was identified, while pluses identify the peak reflectivity in each profile. The heights and times of the data used in the calibration and verification process are indicated by a box.

of turbulence. These are similar to the enhanced Bragg scattering layers (EBSLs)[6] seen in data collected by NCAR's S-band and Ka-band dual-polarization, dual-wavelength Doppler radar (S-PolKa)[7] scanning radar near Barbuda (17.6°N, 61.7°W; Davison et al. 2013) and Addu Atoll (0.5°S, 73.8°E; Davison 2015), which those studies link to strong humidity gradients in the lower troposphere.

d. Estimated maximum error of calibration

There are many unknowns in calibration: choice of proper Z–R relationships, choice of storms to evaluate, accuracy of the surface measurements of precipitation. The radar community is generally very happy to be within ±1.0 dB in their calibration; this is, for instance, the standard used for the National Weather Service nonpolarimetric radars (Ice et al. 2014). We have chosen the Marshall–Palmer Z–R relationship during rainfall

identified as stratiform on the basis of the presence of a bright band, and employed a standard tipping bucket for surface measurements. Our PRC$_{final}$ is −0.11 dB from the PRC determined using the TRMM data and +0.11 dB from the PRC determined using the surface rainfall. Errors in the surface measurement can be covered within ±1 dB of these values. Gage et al. (2002) reported that the calibration of a profiler similar to the Manus one remained stable within 0.4 dB over long periods of time, and we expect the same is true with this one. Taking these factors into account, we are confident that our calibration is accurate to within ±1.5 dB.

6. Final thoughts

We have explored two different methods for calibrating a 915-MHz wind profiling radar after it has been deployed. Both methods relied on the existence of stratiform rain events and their attendant bright bands. One method required a collocated surface rain gauge and at least one relatively long-lived event. The other required many months' worth of observations by a calibrated satellite radar, and for stratiform rain events

---

[6] Originally called "Bragg scattering layers" (BSLs) in pre-2017 work (J. L. Davison, 2017, personal communication).

[7] The S-band portion of S-PolKa transmits at 2.7–2.9 GHz.
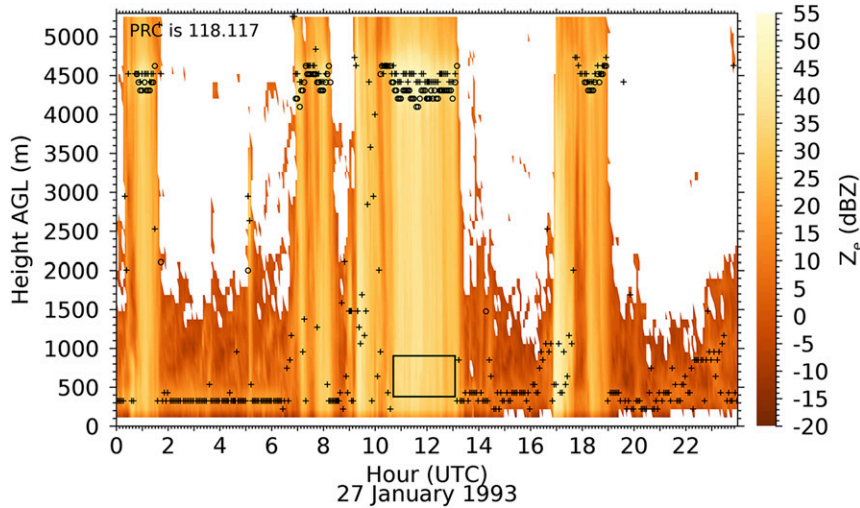
FIG. 11. Equivalent reflectivity factor Z_e during the entirety of 11 Jan 1993. Circles indicate the height of the bright band when it was identified, while pluses identify the peak reflectivity in each profile. The heights and times of the data used to verify the calibration are indicated by a box.

to be common enough that a robust number of bright bands could be observed by both radars. In both methods the combined unspecified parameters, here referred to as the profiler radar constant (PRC), in a simplified version of the radar equation [see (2)] were adjusted to bring the profiler observations into agreement with the transfer standards being used in the calibration.

Calibrating the low height-coverage mode of the Manus profiler, using surface observations during two long-lived stratiform rain events as the transfer standard, yields profiler-based rain accumulations during those events that are within ±4% of the gauge measurements. Calibrating that same mode using bright-band reflectivities from the TRMM PR during its first 3.5 years of operation as the transfer standard yields profiler-based rain accumulations during those events

that are from 0.1% lower to 7.0% higher than the gauge measurements. PRC$_{surface}$ and PRC$_{satellite}$ differ by only 5%, and also yield errors of similar magnitude during two somewhat shorter stratiform rain events, even though contemporaneous profiler and satellite-based bright bands were not employed. We therefore averaged them and used the resulting PRC$_{final}$ to transform uncalibrated SNR from the Manus profiler's low mode into calibrated reflectivity (i.e., equivalent reflectivity factor Z_e) and the structure function parameter of the index of refraction C_n^2.

Implementation details could vary, depending on the needs of the end user. The surface-based technique must be used with diligence; as discussed in section 3, we were extremely careful with timing and with identifying precipitation type, relying on dwell-by-dwell comparisons
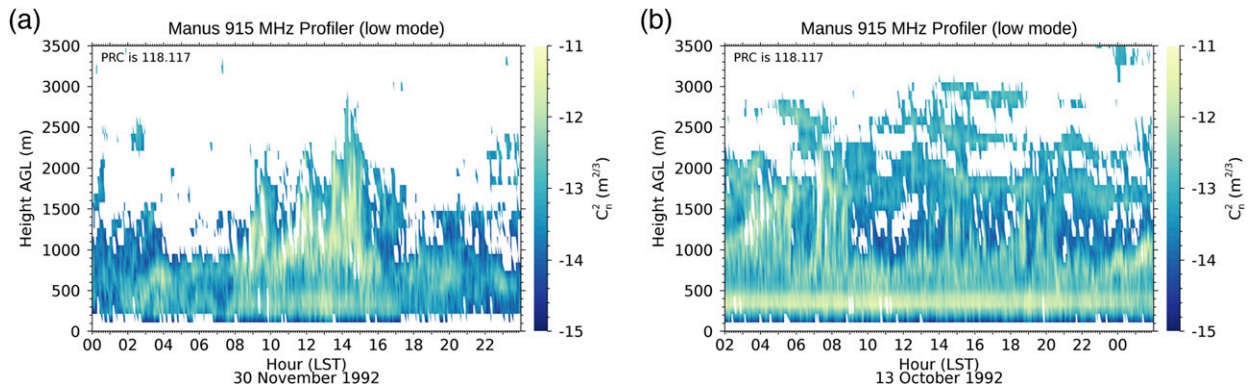
FIG. 12. The evolution of C_n^2 on (a) 30 Nov 1992 (LST) and (b) 13 Oct 1992 (LST), as calculated using the calibrated low-mode reflectivity from the Manus 915-MHz profiler. Local standard time (LST) is UTC + 1000, and sunrise on both days was at approximately 0600 LST.

of precipitation type and fall velocities against tip-by-tip rainfall records to identify the starting and ending accumulation time. The satellite-based technique relies on large numbers of observations from each platform to establish the distributions very robustly before the peaks are matched. This requires careful attention to the long-term operation of the profiler, so that any changes that could affect the SNR can be compensated for. In our case, we were trying to avoid dwell-by-dwell machine or hand editing of the profiler data used in calibration. Such editing might, however, be appropriate for case studies or certain applications of the calibrated data. For instance, in nominally clear-air conditions reflections from birds or insects can yield strong returns that would yield nonatmospheric values of C_n^2. Therefore, some users would be wise to identify outliers and examine the data associated with them. Caution must also be used during extreme echo conditions (cf. McCaffrey et al. 2017). If echoes are too small, the response is nonlinear and hard to apply; in Johnston's experience, this tends to occur for SNR levels less than 10 dB above the Riddle threshold. Conversely, large echoes such as those from hail and extreme rain push the dynamic range of this radar and give underestimates of the SNR. With care, some compensation can be made in these situations.

The work we present here is a proof-of-concept study, and so we have relied on previous research (Gage et al. 2002) for general ideas on the stability of the calibration. However, we can put forth a few additional thoughts on the matter. A prudent data user should continually evaluate instrument performance. Changes to the radar hardware can affect the calibration, so when such changes are made a careful evaluation of the calibration must be done. Antenna degradation is possible in some locations, primarily due to heat, humidity, and/or exposure to salt particles, and could change the calibration factor over time. (At Manus the antenna was kept within an air-conditioned space.) Good equipment maintenance reduces the chances of such issues, and makes it likely that changes can be evaluated soon after they occur. Spot-checking the calibration, perhaps by having a collocated rain gauge and looking for a long-lived well-defined rain event a few times a year, could increase confidence in the calibration or reveal profiler changes. For new installations, we recommend collocating the wind profiler with both a rain gauge and disdrometer for calibration and validation. Using a disdrometer for calibration provides direct estimates of Z and R, removing the need to assume a Z–R relationship.

The goal of this work is to present and compare two calibration techniques. We chose the Marshall–Palmer Z–R relation for our surface-based calibration because it is widely accepted for general use in stratiform rain and we did not want to get into a debate about Z–R relationships, which is a complex topic outside the scope of this work. Many proposed alternative Z–R relations are location or even storm specific, and their derivation often requires drop size distributions (DSDs), which we do not have for this site. Wilson and Brandes (1979) discuss the selection of Z–R relationships and how they vary in time and space, but also assume that in the average Marshall–Palmer constitutes a good average estimation of the rain from stratiform rain. We make the same assumption, which is supported by the independent results obtained using the TRMM data.

There was a 3.5-yr gap between the end of the profiler data and the start of the TRMM data used for the satellite-based calibration. While the lack of overlap expanded the calibration options, it also raises questions about the possibility that slowly varying atmospheric signals might affect brightband reflectivities and contaminate the calibration. Given Manus's location in the west Pacific warm pool, and the fact that multiyear records would serve to filter signals related intraseasonal variability such as the Madden–Julian oscillation, ENSO is the most obvious signal of concern in this instance. Our satellite-based calibration assumes that brightband reflectivities over Manus are independent of ENSO. In appendix B we have used the profiler and TRMM data together with time series from the Twentieth Century Reanalysis, version 2c (20CRv2c; Compo et al. 2011; Compo et al. 2015; Giese et al. 2016), to evaluate some brightband relationships that have been reported in the literature. We decided that while the heights of bright bands over Manus may be affected by ENSO, their reflectivities appear not to be. We hope to conduct a more detailed and thorough analysis of the effect of ENSO on brightband characteristics over Manus Island in the future.

There are also avenues for further research into radar-related aspects of the calibration. For instance, wind profilers can provide data with short-enough time scales that some examination of the microphysics of the events could be possible. These details could explain the gate-to-gate spread of the data. Breakup and coalescence do not affect the liquid water content, only the drop size distributions, but advection and evaporation do affect the liquid water content by removing drops from or reducing drop size in the volumes examined. While our premise is that these effects average out by integrating over the storm, interested researchers could look into individual rain events and do detailed studies along these lines. Similarly, because of similarity of the rain in gates 4–8 to that in the lower gates it could be possible to calibrate the lowest three gates by using different

calibration constants. In these lowest gates there is a nonlinear response due to the gradient in the r^2 term along the radial dimension of the volume that occurs when the range is on the order of the pulse width (cf. Johnston et al. 2002). Finally, repeating the surface-based calibration with other Z–R relationships could provide interesting results about the variation and applicability of using Z–R relationships to measure rain.

This research was as much an exercise in comparing methods as it was an exercise in postdeployment calibration, and we have made an argument for a calibration of this particular profiler that combines the results from both methods. The good agreement between our two methods, even in the absence of temporal overlap between the profiler-based statistics and the satellite-based statistics, increases the number of options available to those wishing to calibrate other profilers. If the requirements for both methods are met, do we recommend expending the effort to try both methods and merge their answers? The results of the two methods were so close that if the requirements for only one of the methods were met, or if other considerations suggested using only one method, we believe the result from either would be robust as long as one of the following conditions were met: multiple events were used for the surface-based method, or many months were used for the satellite-based method. What about calibrating profilers located in regions where stratiform rain is rare? If good surface-based rain measurements are available and the precipitation type can be reliably determined, a different Z–R relationship could be employed with the basic method described in section 3.

This calibration means that low-mode data from the Manus profiler can now be employed for new types of research. In 1996, the U.S. Department of Energy established the first tropical western Pacific (TWP) Atmospheric Radiation Measurement (ARM) facility at Momote Airport (Long et al. 2013). The profiler Z_e could be used in conjunction with reflectivities from ARM data for precipitation studies, while C_n^2 could be used to study turbulent structures during nonprecipitating periods in combination with ARM radiosonde profiles. Calibrating other TPPN profilers would leverage existing datasets and effectively increase the amount of high-resolution information available in the in the lower troposphere over the tropical Pacific.

APPENDIX A

PDAprecipAll Software Algorithms

This appendix briefly describes the processing steps and algorithms used by the software package PDAprecipAll to apply corrections to the profiler data that were processed and recorded at the site in real time. That original on-site data processing [described in Carter et al. (1995) and Riddle et al. (2012)] analyzed each range gate independently. It computed the moments for each range gate (SNR, radial velocity, spectral width, and noise level) from the average power spectrum and saved them, together with the associated spectrum. PDAprecipAll uses the same basic methods with a couple of additional steps.

PDAprecipAll starts with the power spectra saved by the real-time software for one dwell. Contoured spectra from all range gates during one low-mode dwell of the Manus profiler, as displayed by the Lap-XM console program, are shown in Fig. A1. These data are from 1425:43 UTC 14 December 1992, during one of the stratiform rain events used for calibration; the high SNRs associated with the bright band are seen at about 4500 m, as are the large downward (positive) velocities of the rain below it. Also visible is frequency aliasing of the signal in ranges below
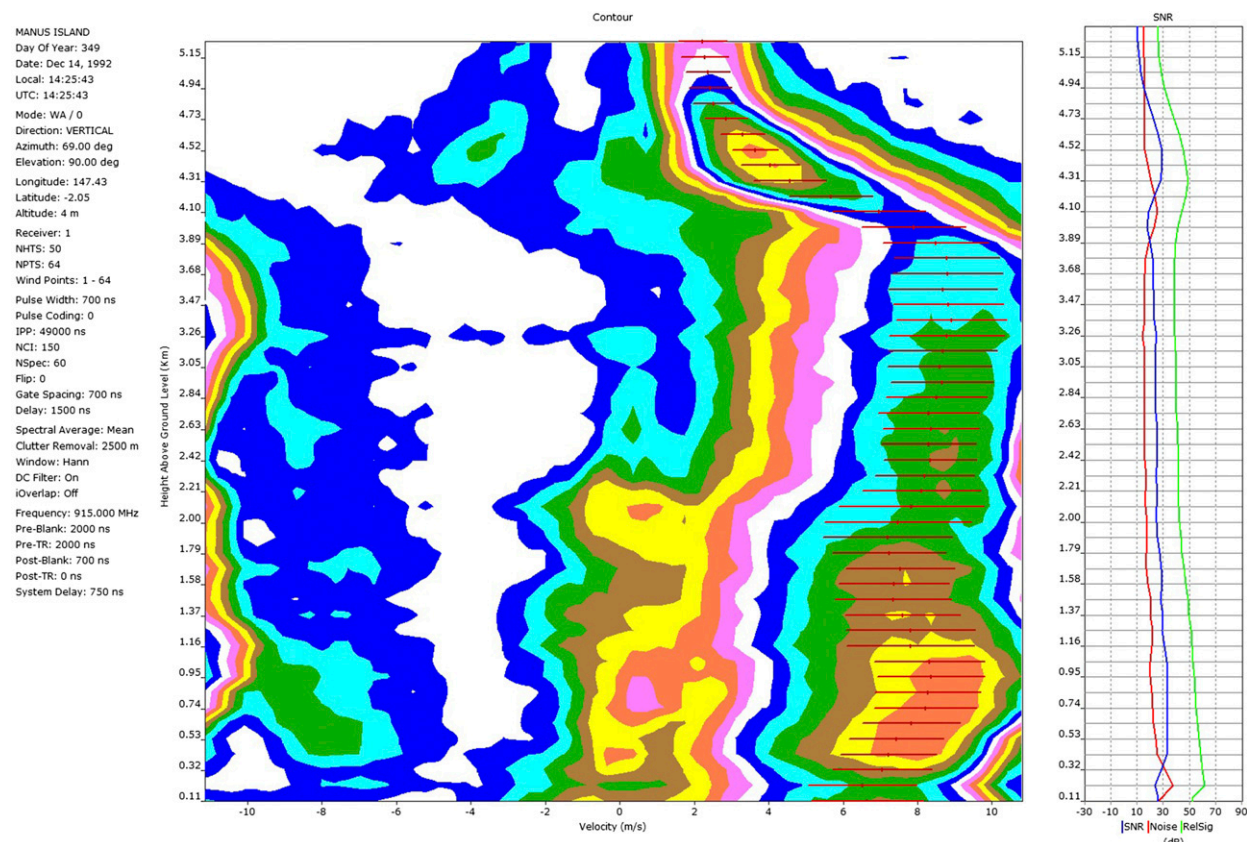
FIG. A1. A screen shot of one low-mode vertical dwell from the Manus profiler t 1425:43 UTC 14 Dec 1992. The text on the left shows that NPTS = 64 and NCI = 150. The central plot shows the power spectra at each range gate. These have been contoured to show the entire signal. The first contour is 1 dB above the mean noise level for that range, and the contour interval is 3 dB. The red crosses at each range gate indicate the mean velocity (vertical line) and spectral width (horizontal line). The velocity is radial Doppler velocity (m s^{-1}), with positive values denoting motion toward the radar. The right plot shows mean signal (green), noise (red), and SNR (blue) at each range gate, using a dB scale.

4.31 km, where the contours wrap from ~11 to ~−11 m s^{-1}. The noise in wind profilers is thermal noise from the antenna and receiver, and is independent of range [see (8) in Gage and Balsley (1978)]. However in the accompanying plot of noise, the noise level is not constant with range.

PDAprecipAll's first step is to recompute the moments at each range. This procedure is very similar to the real-time software. Starting with the power spectrum, the average noise level is determined using the Hildebrand and Sekhon (1974) method. The size of the spectrum is then doubled by copying the data from each side of the spectrum and placing it on the end of the opposite side. This unwraps the aliased signal. Next PDAprecipAll deviates from the real-time software by applying a time domain averaging (TDA) filter correction to the signal points [Gage and Balsley 1978, their (7)], which are those values above the mean noise level. The TDA filter depends on the spectral point frequency n, the number of points in the spectra (NPTS),

and the number of coherent integrations (NCI), as seen in Rastogi [1983, their (4)], here written as

$$G_{\text{TDA}}(n) = \frac{\sin^2\left(\dfrac{\pi n}{\text{NPTS}}\right)}{\text{NCI}^2 \sin^2\left(\dfrac{\pi n}{\text{NPTS} \times \text{NCI}}\right)}. \qquad \text{(A1)}$$

Figure A2a shows this function for the parameters used in Fig. A1 (NPTS = 64, NCI = 150). These are plotted in linear units, since all the manipulations of the power spectra are done in the linear power domain. At the Nyquist frequency (point 32 in Fig A2), G_{TDA} is down by a factor of 0.4 (−3.92 dB). To correct for this filter effect, the signal part of the power spectrum, consisting of the parts of the power spectrum above the mean noise level, is multiplied by the inverse of the filter function. Figure A2b shows this correction function [the inverse of $G_{\text{TDA}}(n)$], limited to a multiplication factor of 20.

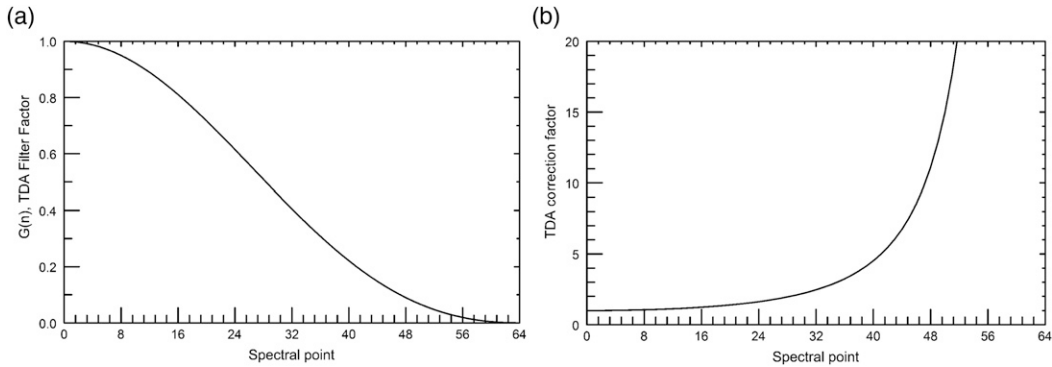PDAprecipAll's second additional step is determination of the average noise level for the dwell. For reasons

FIG. A2. The (a) TDA filter function and (b) TDA correction function. The functions are symmetric, so only one side of the spectral response is shown. Point 0 corresponds to a frequency of 0. In (a) the Nyquist point is 32, and points greater than 32 represent frequency aliased signals. In (b) only correction function values ≤ 20 are shown. There is a zero in the filter function at point 64, so the correction function becomes very large as it approaches the singularity at point 64.

that are beyond the scope of this paper, the signal leaks into the noise and the noise level for each individual gate is not determined well, leading to noise that is not independent of range (cf. Fig. A1). To determine the average noise level for the dwell, the power spectra for the range gates with the smallest total power are combined into a single array. The number of ranges used in the array varies with the dwell; at least eight are used, along with additional range gates that have SNR less than 8 dB above the Riddle threshold (Riddle et al. 2012). This array is then processed using the Hildebrand and Sekhon (1974) method to determine the average noise level. The SNR at each gate is than normalized to the average noise level.

These two additions to the moment processing have a large effect on the SNR values, which are then used to compute the reflectivity. Figure A3 shows how the values change for the data shown in Fig. A1. The SNR (Fig. A3b) is affected the most by the reprocessing of the power spectra. Most of this is caused by the improved noise level; PDAprecipAll has removed small-scale perturbations caused by fluctuations in the noise level. The velocity shows a minor increase, caused by the removal of the TDA filter effect. For the calibration work presented here this is not crucial, but for some applications this might be an important source of bias. Figure A3b, in which the SNR values have been converted to relative reflectivity by adding $20 \times \log[\text{range (km)}]$ to the SNR, illustrates how reprocessing of the moments affects the reflectivities. This example shows the bright band moving down with the reprocessing, which is not the usual case (cf. Fig. 6d).

Figure A4 visualizes, in multiple ways, the ratio of the revised SNR to the original SNR at gates heights

4–50 for all four stratiform events used in the Manus calibration. The changes to SNR can be many dB (Fig. A4a). Since reflectivity is proportional to SNR, the differences in SNR shown in Fig. A4 correspond to changes in reflectivity. The corrections are most important at the lowest heights and near the bright band (Fig. A4c). For many spectra, the change is less than 2 dB (Fig. A4b). At the lowest gates, the changes can be much larger than the average (Fig. A4c), so it is important to make the corrections.

After the SNR values have been computed, PDAprecipALL uses (2) to compute the reflectivity assuming both Rayleigh scatter from liquid precipitation Z_e and Bragg scatter from clear air C_n^2. The SNR value is compared with the Riddle threshold (Riddle et al. 2012) to determine if a signal is present. The radar reflectivity factor, $10 \times \log(Z_e)$, is used to classify the signals into different classes based on the cluster analysis of Williams et al. (2000). This results in three classes: no echo, clear-air echo, and precipitation echo.

The Z_e value in logarithmic units (dBZ) is used to estimate the rain rate for the each height of the dwell. Four different Z–R relationships are used (Zhang et al. 2011), with Z the reflectivity in linear units (mm^6 m^{-3}) and R the rain rate (mm h^{-1}): convective ($Z = 300R^{1.4}$), stratiform ($Z = 200R^{1.6}$; the Marshall-Palmer Z–R relationship; Marshall et al. 1955), warm rain ($Z = 230R^{1.25}$), and snow at surface ($Z = 75R^{2.0}$). If the echo is classified as precipitation, the rain rate is converted to an accumulation amount by multiplying it by the time to the next observation. This accumulation is added to the accumulation for the dataset being analyzed.

After the dwell has been analyzed, the results for each range are output into an output file for research use. The
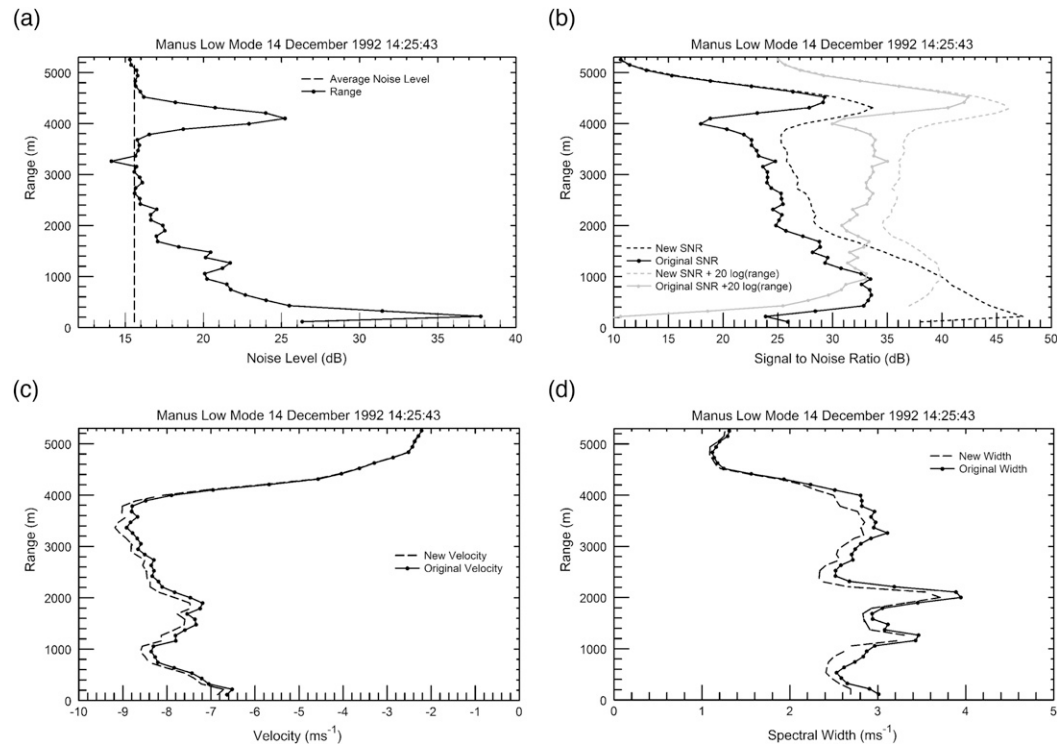
FIG. A3. Profiles computed by PDAprecipAll compared with the originals, all from the Manus profiler low-mode vertical scan at 1425:43 UTC 14 Dec 1992: (a) noise, (b) SNR, (c) radial velocity (positive motion is upward), and (d) spectral width. The gray lines in (b) are proportional to reflectivity, computed for gates 4–50 only.

locations and values of the maximum reflectivity factors (MAXR) are output to a different file for use in locating the peak reflectivity. Two pairs of reflectivity and height are output for each profile: the maximum reflectivity for the entire profile and the maximum reflectivity above 3 km.

APPENDIX B

ENSO's Impact on Bright Bands over Manus

Our satellite calibration uses Manus profiler data from July 1992 to August 1994 and TRMM data over Manus from January 1998 to July 2001. ENSO is a major signal in the tropical west Pacific and was in a multiple phases during these two different time periods. To evaluate the potential impact of using brightband data during different ENSO phases on our satellite-based calibration, we have examined relationships between various ENSO indicators, freezing levels from a global reanalysis, and brightband heights and reflectivities from the Manus profiler and TRMM. It is not our intent to present a comprehensive research study in this appendix, but to develop some lines of evidence to address concerns that the temporal mismatch between the profiler and TRMM

data may cause serious problems with our satellite-based calibration results.

The profiler and TRMM time series we are using are rather short for assessing relationships to a phenomenon that varies on multiyear time scales. To do this evaluation we need a consistent, uninterrupted time series that is relevant to brightband properties and suitable for long-term statistics. Global analyses are an obvious choice. Brightband heights or reflectivities are not standard output from such analyses but temperature and geopotential height are, and it is well established that the bright band occurs somewhat below the 0°C level (e.g., Hooper and Kippax 1950; White et al. 2002). We obtained daily time series of temperature and geopotential height at the 2.0° × 2.0° grid point nearest Manus (2.0°S, 148.0°E) from the 20CRv2c (Compo et al. 2011, 2015; Giese et al. 2016). The time series covered the period 1985–2010,[8] and extended vertically from 650 to 450 hPa in 50-hPa increments. From 1986 to 2010, the freezing

---

[8] The focus of our long-term analysis was 1986–2010, providing a several-year bracket before and after the profiler and TRMM time series. The 1985 values were obtained for the purposes of multimonth averages centered on January 1986.
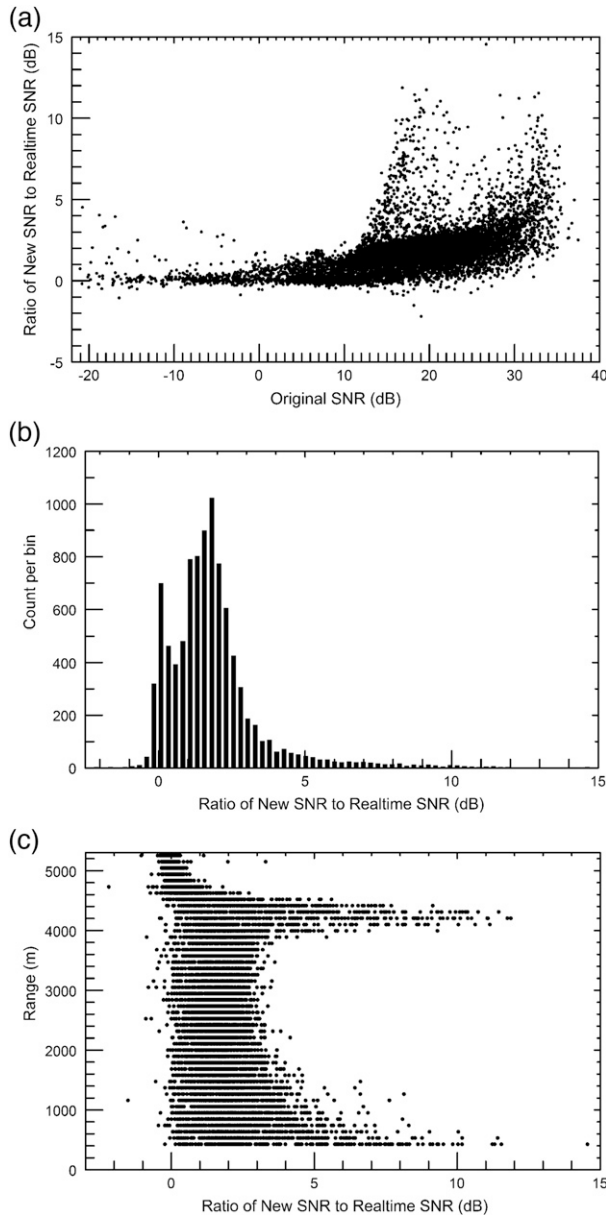
(a)

(b)

(c)

FIG. A4. The ratio of the revised SNR to the original SNR using data from range gates 4–50 during the four events used for calibration and verification. There are 9165 points represented in each plot. The arithmetic mean is 1.78 dB, the median value is 1.62 dB, and the standard deviation is 1.5 dB. (a) The scatter of the points. (b) The histogram of the ratio, with 0.25-dB bins. (c) How the SNRs are changed with height.

(a)

(b)

FIG. B1. Monthly mean values of the freezing level at the grid point nearest to Manus (2.0°S, 148.0°W; solid line), obtained via linear interpolation from daily temperature and geopotential height from 20CRv2c, together with monthly mean brightband heights from (a) the Manus profiler and (b) the $0.5° \times 0.5°$ TRMM grid point over Manus. The July 1998 TRMM brightband height is circled.

The first question is whether 20CRv2C freezing levels are a reasonable proxy for brightband heights. Monthly values of the freezing level over Manus are shown together with monthly brightband heights from the profiler and from the TRMM grid point over Manus in Fig. B1. High-frequency variability is more apparent in brightband heights than in freezing levels, but the paired time series also track each other to some extent. The correlation between the freezing level and the brightband height is larger for the 1992–94 period (0.41, which is significant) than for the 1998–2001 period (0.27). However, the July 1998 TRMM brightband height (4073 m) is 153.7 m (about one standard deviation) below the next lowest value (4226.7 m in August 2000). Pearson's correlation coefficient is known to be sensitive to outliers, and if the July 1998 TRMM brightband height is omitted the 1998–2001 correlation jumps to 0.45, which is significant.

The difference between the freezing level over Manus and the brightband heights, also called the height

level lay between 500 and 550 hPa on 135 days and between 550 and 600 hPa on all others. We used linear interpolation to compute the height of the freezing level on each day, as per Bradley et al. (2009), and then calculated monthly means and constructed 2- and 3-month running mean time series centered January 1986–December 2010.
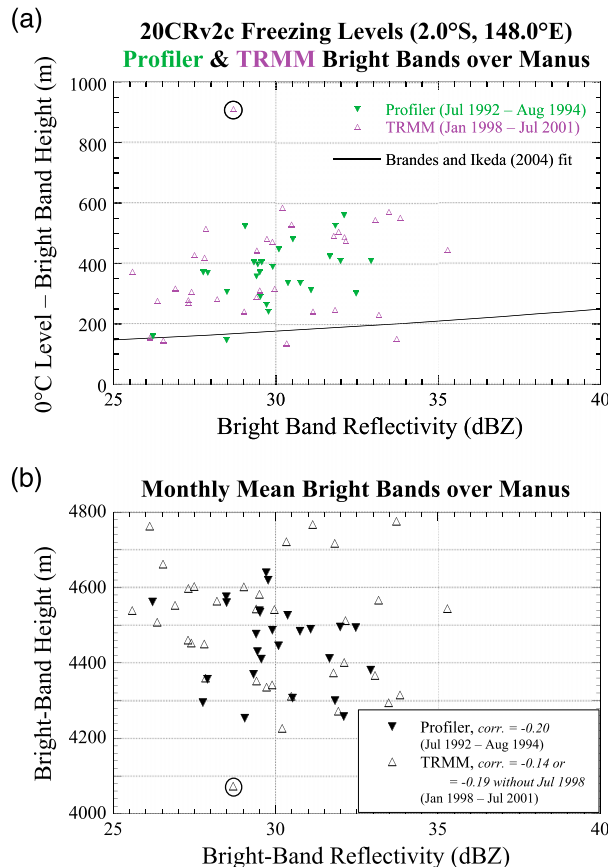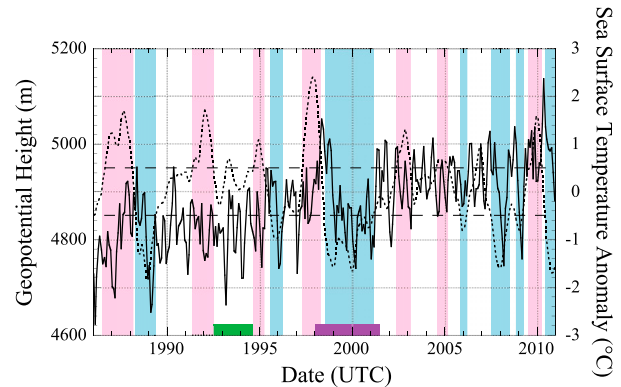
(a)

(b)

FIG. B2. (a) The difference between monthly mean 20CRv2c freezing levels over Manus and monthly mean brightband heights from the Manus profiler and from TRMM, i.e., the brightband height depression, as a function of brightband reflectivity. Also shown is the line fit by Brandes and Ikeda (2004) to data extracted from observations by Fabry and Zawadzki (1995). (b) Monthly mean brightband heights from both the Manus profiler and TRMM as a function of brightband reflectivity. In both panels, the July 1998 TRMM brightband height is circled.

FIG. B3. Monthly mean values of the freezing level at the 20CRv2c grid point nearest to Manus (2.0°S, 148.0°W; solid line). Green and purple bars along the bottom axis highlight the period encompassed by profiler and TRMM brightband data, respectively. Also plotted are monthly values of the ONI (dotted line), each of which is a 3-month running mean value of SST anomalies over the Niño 3.4 region (5°N–5°S, 120°–170°W). Periods during which the ONI was outside the ±0.5°C threshold for at least 5 consecutive months are shaded pink to indicate warm events and light blue to indicate cold events.

depression, is shown in Fig. B2a as a function of brightband reflectivity. The profiler reflectivity values are calculated using PRC_{final} [i.e., (4)], which is the average of $PRC_{surface}$ and $PRC_{satellite}$. The profiler and TRMM height depressions form clouds that overlap each other and cover similar ranges as the values for comparable maximum reflectivities in Brandes and Ikeda (2004, their Fig. 3a). The mean height depression is 370 m for the profiler time series and 373 m for the TRMM time series. These are larger than the 101 m found in the first known comparison of the two quantities (Hooper and Kippax 1950) using data from southern England. They are also larger than values along the line fit by Brandes and Ikeda (2004, their Fig. 3a) to data extracted from observations near Montreal by Fabry and Zawadzki (1995), which range

from 147 m for maximum brightband reflectivity equaling 25 dBZ to 209 m for maximum reflectivity equal to 35 dBZ. However, the mean depressions as well as the individual monthly values generally fall within the envelope of "sampling of depressions from field experiments conducted in Florida and Brazil" shown in Brandes and Ikeda's Fig. 3a. The mean depressions are also comparable to the ~300-m zonally averaged mean difference at 2.5°S that Thurai et al. (2003) found when comparing four years of TRMM brightband heights with the annual mean freezing level specified by International Telecommunication Union Radiocommunication Sector (ITU-R) recommendation P.839-3 (ITU-R 2001). Figure B2a shows that the profiler brightband depressions as well as the TRMM ones vary with brightband reflectivity in a similar manner to other studies' results. This, coupled with the correlations between the observed bright bands and the freezing levels, gives us confidence in the reasonableness of using 20CRv3c freezing levels as a proxy for brightband heights.

The second question is whether freezing heights show variability related to ENSO. The monthly time series of the freezing level is shown in Fig. B3 together with the Oceanic Niño Index (ONI; CPC 2018). The ONI, which is used operationally by NOAA to identify warm (El Niño) and cold (La Niña) phases of ENSO, is the 3-month running mean value of SST anomalies over the Niño 3.4 region (5°N–5°S, 120°–170°W). Diaz et al. (2003), Bradley et al. (2009), and others have documented positive correlations between spatially averaged freezing-level height

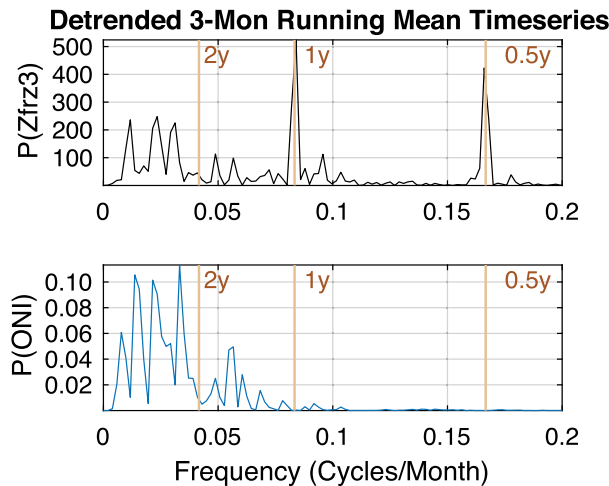## Detrended 3-Mon Running Mean Timeseries

FIG. B4. Power spectra of detrended monthly time series (1986–2010) of the 3-month running mean 20CRv2c (top) freezing level near Manus and (bottom) the ONI. Power at frequencies greater than 0.2 cycles per month is negligible.

and ENSO, often strongest with freezing level lagging by months, while Harris et al. (2000) found that freezing levels over the Manus region during 1998 were higher than the 1979–98 mean freezing-level heights from the NCEP reanalysis. The monthly mean 20CRv2c freezing level at the single grid point nearest Manus exhibits considerable high-frequency variability, but there are visual signs of a lagged relationship with warm and cold ENSO events. Spectral analysis of the detrended time series (Fig. B4) shows that while the Manus freezing-level height contains power at ENSO-like time scales (7.1, 3.6, and 2.7 years), the largest power is at 6- and 12-month time scales. The highest positive correlations between the ONI and 3-month running mean values of the 20CRv2c freezing-level heights over Manus occur when freezing level lags the ONI by 7 months ($r = 0.26$, which is significant).

The freezing heights over Manus do have variability on ENSO, yearly, and half-yearly time scales, and their temporal correlation to the brightband heights from both the profiler and TRMM suggests that those brightband heights may also have variability on those time scales. (The short duration of the brightband time series, and the gaps in the TRMM data, preclude meaningful lagged correlation analysis.) However, in our satellite calibration we only use height as a discriminant as we identify bright bands in the profiler data. The remaining question is whether brightband reflectivities over Manus are affected by ENSO, and we have no long-term proxy time series for those reflectivities. For both the profiler and the TRMM data, brightband heights and the brightband reflectivities (Fig. B2b) exhibit only weak negative correlations. From this we

infer, but do not prove, that even though the brightband heights may be affected by ENSO, the brightband reflectivities appear to be independent of ENSO.

REFERENCES

Angevine, W. M., W. L. Ecklund, D. A. Carter, K. S. Gage, and K. P. Moran, 1994: Improved radio acoustic sounding techniques. *J. Atmos. Oceanic Technol.*, **11**, 42–49, https://doi.org/10.1175/1520-0426(1994)011<0042:IRAST>2.0.CO;2.

Awaka, J., T. Iguchi, and K. Okamoto, 2009: TRMM PR standard algorithm 2A23 and its performance on bright band detection. *J. Meteor. Soc. Japan*, **87A**, 31–52, https://doi.org/10.2151/jmsj.87A.31.

Bianco, L., D. Cimini, F. S. Marzano, and R. Ware, 2005: Combining microwave radiometer and wind profiler radar measurements for high-resolution atmospheric humidity profiling. *J. Atmos. Oceanic Technol.*, **22**, 949–965, https://doi.org/10.1175/JTECH1771.1.

Bradley, R. S., F. T. Keimig, H. F. Diaz, and D. R. Hardy, 2009: Recent changes in freezing level heights in the tropics with implications for the deglacierization of high mountain regions. *Geophys. Res. Lett.*, **36**, L17701, https://doi.org/10.1029/2009GL037712.

Brandes, E. A., and K. Ikeda, 2004: Freezing-level estimation with polarimetric radar. *J. Appl. Meteor.*, **43**, 1541–1553, https://doi.org/10.1175/JAM2155.1.

Campbell Scientific, 2004: TE525 tipping bucket rain gauge instruction manual. Campbell Scientific Doc., 14 pp.

Carter, D. A., K. S. Gage, W. L. Ecklund, W. M. Angevine, P. E. Johnston, A. C. Riddle, J. Wilson, and C. R. Williams, 1995: Developments in UHF lower tropospheric wind profiling at NOAA's Aeronomy Laboratory. *Radio Sci.*, **30**, 977–1001, https://doi.org/10.1029/95RS00649.

Chadwick, R. B., and K. P. Moran, 1980: Long-term measurements of C_n^2 in the boundary layer. *Radio Sci.*, **15**, 355–361, https://doi.org/10.1029/RS015i002p00355.

Ciesielski, P. E., L. M. Hartten, and R. H. Johnson, 1997: Impacts of merging profiler and rawinsonde winds on TOGA COARE analyses. *J. Atmos. Oceanic Technol.*, **14**, 1264–1279, https://doi.org/10.1175/1520-0426(1997)014<1264:IOMPAR>2.0.CO;2.

CPC, 2018: Cold & warm episodes by season. CPC, http://origin.cpc.ncep.noaa.gov/products/analysis_monitoring/ensostuff/ONI_v5.php.

Compo, G. P., and Coauthors, 2011: The Twentieth Century Reanalysis project. *Quart. J. Roy. Meteor. Soc.*, **137**, 1–28, https://doi.org/10.1002/qj.776.

——, and Coauthors, 2015: NOAA/CIRES Twentieth Century Global Reanalysis, version 2c. National Center for Atmospheric Research Computational and Information Systems Laboratory Research Data Archive, accessed 18 June 2018, https://doi.org/10.5065/D6N877TW.

Davison, J. L., 2015: A filter for removing sidelobe artifacts in Bragg scattering layer (BSL) analysis for S-band radar. *J. Atmos. Oceanic Technol.*, **32**, 1289–1297, https://doi.org/10.1175/JTECH-D-15-0033.1.

——, R. M. Rauber, and L. Di Girolamo, 2013: A revised conceptual model of the tropical marine boundary layer. Part II: Detecting relative humidity layers using Bragg scattering from S-band radar. *J. Atmos. Sci.*, **70**, 3025–3046, https://doi.org/10.1175/JAS-D-12-0322.1.

Diaz, H. F., J. K. Eischeid, C. Duncan, and R. S. Bradley, 2003: Variability of freezing levels, melting season indicators, and

snow cover for selected high-elevation and continental regions in the last 50 years. *Climatic Change*, **59**, 33–52, https://doi.org/10.1023/A:1024460010140.

Doviak, R. J., and D. S. Zrnić, 1993: *Doppler Radar and Weather Observations*. 2nd ed. Academic Press, 562 pp.

Fabry, F., and I. Zawadzki, 1995: Long-term radar observations of the melting layer of precipitation and their interpretation. *J. Atmos. Sci.*, **52**, 838–851, https://doi.org/10.1175/1520-0469(1995)052<0838:LTROOT>2.0.CO;2.

Funk, A., C. Schumacher, and J. Awaka, 2013: Analysis of rain classifications over the tropics by version 7 of the TRMM PR 2A23 algorithm. *J. Meteor. Soc. Japan*, **91**, 257–272, https://doi.org/10.2151/jmsj.2013-302.

Gage, K. S., and B. B. Balsley, 1978: Doppler radar probing of the clear atmosphere. *Bull. Amer. Meteor. Soc.*, **59**, 1074–1093, https://doi.org/10.1175/1520-0477(1978)059<1074:DRPOTC>2.0.CO;2.

——, C. R. Williams, W. L. Clark, P. E. Johnston, and D. A. Carter, 2002: Profiler contributions to Tropical Rainfall Measuring Mission (TRMM) ground validation field campaigns. *J. Atmos. Oceanic Technol.*, **19**, 843–863, https://doi.org/10.1175/1520-0426(2002)019<0843:PCTTRM>2.0.CO;2.

Giese, B. S., H. F. Seidel, G. P. Compo, and P. D. Sardeshmukh, 2016: An ensemble of ocean reanalyses for 1815–2013 with sparse observational input. *J. Geophys. Res. Oceans*, **121**, 6891–6910, https://doi.org/10.1002/2016JC012079.

Görsdorf, U., and V. Lehmann, 2000: Enhanced accuracy of RASS-measured temperatures due to an improved range correction. *J. Atmos. Oceanic Technol.*, **17**, 406–416, https://doi.org/10.1175/1520-0426(2000)017<0406:EAORMT>2.0.CO;2.

Gossard, E. E., 1977: Refractive index variance and its height distribution in different air masses. *Radio Sci.*, **12**, 89–105, https://doi.org/10.1029/RS012i001p00089.

——, D. E. Wolfe, K. P. Moran, R. A. Paulus, K. D. Anderson, and L. T. Rogers, 1998: Measurement of clear-air gradients and turbulence properties with radar wind profilers. *J. Atmos. Oceanic Technol.*, **15**, 321–342, https://doi.org/10.1175/1520-0426(1998)015<0321:MOCAGA>2.0.CO;2.

Gutzler, D. S., and L. M. Hartten, 1995: Daily variability of lower tropospheric winds over the tropical western Pacific. *J. Geophys. Res.*, **100**, 22 999–23 008, https://doi.org/10.1029/95JD01879.

Harris, G. N., Jr., K. P. Bowman, and D.-B. Shin, 2000: Comparison of freezing-level altitudes from the NCEP reanalysis with TRMM Precipitation Radar brightband data. *J. Climate*, **13**, 4137–4148, https://doi.org/10.1175/1520-0442(2000)013<4137:COFLAF>2.0.CO;2.

Hartten, L. M., 1998: Reconciliation of surface and profiler winds at ISS sites. *J. Atmos. Oceanic Technol.*, **15**, 826–834, https://doi.org/10.1175/1520-0426(1998)015<0826:ROSAPW>2.0.CO;2.

——, and P. A. Datulayta, 2004: Seasonal and interannual variations in the daily cycle of winds over the Galápagos. *J. Climate*, **17**, 4522–4530, https://doi.org/10.1175/3217.1.

——, and P. E. Johnston, 2014: Stratocumulus-topped marine boundary layer processes revealed by the absence of profiler reflectivity. *J. Appl. Meteor. Climatol.*, **53**, 1775–1789, https://doi.org/10.1175/JAMC-D-12-0308.1.

Hildebrand, P. H., and R. S. Sekhon, 1974: Objective determination of the noise level in Doppler spectra. *J. Appl. Meteor.*, **13**, 808–811, https://doi.org/10.1175/1520-0450(1974)013<0808:ODOTNL>2.0.CO;2.

Hooper, J. E. N., and A. A. Kippax, 1950: The bright band—A phenomenon associated with radar echoes from falling rain. *Quart. J. Roy. Meteor. Soc.*, **76**, 125–132, https://doi.org/10.1002/qj.49707632803.

Hou, A. Y., and Coauthors, 2014: The Global Precipitation Measurement Mission. *Bull. Amer. Meteor. Soc.*, **95**, 701–722, https://doi.org/10.1175/BAMS-D-13-00164.1.

Ice, R. L., A. K. Heck, J. G. Cunningham, and W. D. Zittel, 2014: Challenges of polarimetric weather radar calibration. *Eighth European Conf. on Radar in Meteorology and Hydrology*, Garmisch-Partenkirchen, Germany, DWD, 8.1.

ITU-R, 2001: Rain height model for prediction methods. ITU-R Rep. P.839-3, 2 pp., https://www.itu.int/rec/R-REC-P.839-3-200102-S/en.

Johnson, R. H., P. E. Ciesielski, and K. A. Hart, 1996: Tropical inversions near the 0°C level. *J. Atmos. Sci.*, **53**, 1838–1855, https://doi.org/10.1175/1520-0469(1996)053<1838:TINTL>2.0.CO;2.

Johnston, P. E., L. M. Hartten, C. H. Love, D. A. Carter, and K. S. Gage, 2002: Range errors in wind profiling caused by strong reflectivity gradients. *J. Atmos. Oceanic Technol.*, **19**, 934–953, https://doi.org/10.1175/1520-0426(2002)019<0934:REIWPC>2.0.CO;2.

——, J. R. Jordan, A. B. White, D. A. Carter, D. M. Costa, and T. E. Ayers, 2017: The NOAA FM-CS snow-level radar. *J. Atmos. Oceanic Technol.*, **34**, 249–267, https://doi.org/10.1175/JTECH-D-16-0063.1.

Keenan, T., and Coauthors, 2000: The Maritime Continent Thunderstorm Experiment (MCTEX): Overview and some results. *Bull. Amer. Meteor. Soc.*, **81**, 2433–2455, https://doi.org/10.1175/1520-0477(2000)081<2433:TMCTEM>2.3.CO;2.

Kummerow, C., W. Barnes, T. Kozu, J. Shiue, and J. Simpson, 1998: The Tropical Rainfall Measuring Mission (TRMM) sensor package. *J. Atmos. Oceanic Technol.*, **15**, 809–817, https://doi.org/10.1175/1520-0426(1998)015<0809:TTRMMT>2.0.CO;2.

——, and Coauthors, 2000: The status of the Tropical Rainfall Measuring Mission (TRMM) after two years in orbit. *J. Appl. Meteor.*, **39**, 1965–1982, https://doi.org/10.1175/1520-0450(2001)040<1965:TSOTTR>2.0.CO;2.

Long, C. N., and Coauthors, 2013: ARM research in the equatorial western Pacific: A decade and counting. *Bull. Amer. Meteor. Soc.*, **94**, 695–708, https://doi.org/10.1175/BAMS-D-11-00137.1.

Marshall, J. S., W. Hitschfeld, and K. L. S. Gunn, 1955: Advances in radar weather. *Advances in Geophysics*, Vol. 2, Academic Press, 1–56.

Matuura, N., Y. Masuda, H. Inuki, S. Kato, S. Fukao, T. Sato, and T. Tsuda, 1986: Radio acoustic measurement of temperature profile in the troposphere and stratosphere. *Nature*, **323**, 426–428, https://doi.org/10.1038/323426a0.

McCaffrey, K., L. Bianco, and J. M. Wilczak, 2017: Improved observations of turbulence dissipation rates from wind profiling radars. *Atmos. Meas. Tech.*, **10**, 2595–2611, https://doi.org/10.5194/amt-10-2595-2017.

McPhaden, M. J., and Coauthors, 1998: The Tropical Ocean-Global Atmosphere observing system: A decade of progress. *J. Geophys. Res.*, **103**, 14 169–14 240, https://doi.org/10.1029/97JC02906.

Miller, E. R., and A. C. Riddle, 1994: TOGA COARE Integrated Sounding Station data report—Volume IA revised edition. UCAR Rep., 87 pp.

Nath, D., M. Venkat Ratnam, A. K. Patra, B. V. Krishna Murthy, and S. V. Bhaskar Rao, 2010: Turbulence characteristics over tropical station Gadanki (13.5°N, 79.2°E) estimated using high-resolution GPS radiosonde data. *J. Geophys. Res.*, **115**, D07102, https://doi.org/10.1029/2009JD012347.

National Weather Service, 1998: Automated Surface Observing System: ASOS user's guide. NOAA Rep., 89 pp., http://www.nws.noaa.gov/asos/pdfs/aum-toc.pdf.

Parsons, D., and Coauthors, 1994: The Integrated Sounding System: Description and preliminary observations from TOGA COARE. *Bull. Amer. Meteor. Soc.*, **75**, 553–567, https://doi.org/10.1175/1520-0477(1994)075<0553:TISSDA>2.0.CO;2.

Rastogi, P. K., 1983: A note on the use of coherent integration in periodogram analysis of MST radar signals. *URSI/SCOSTEP Workshop on Technical Aspects of MST Radar*, Urbana, IL, University of Illinois at Urbana–Champaign, 509–512.

Réchou, A., T. N. Rao, O. Bousquet, M. Plu, and R. Decoupes, 2014: Properties of rainfall in a tropical volcanic island deduced from UHF wind profiler measurements. *Atmos. Meas. Tech.*, **7**, 409–418, https://doi.org/10.5194/amt-7-409-2014.

Riddle, A. C., L. M. Hartten, D. A. Carter, P. E. Johnston, and C. R. Williams, 2012: A minimum threshold for wind profiler signal-to-noise ratios. *J. Atmos. Oceanic Technol.*, **29**, 889–895, https://doi.org/10.1175/JTECH-D-11-00173.1.

Rogers, R. R., S. A. Ethier, W. L. Ecklund, D. A. Carter, and K. S. Gage, 1993: Research applications of a boundary-layer wind profiler. *Bull. Amer. Meteor. Soc.*, **74**, 567–580, https://doi.org/10.1175/1520-0477(1993)074<0567:RAOABL>2.0.CO;2.

Schafer, R., P. T. May, T. D. Keenan, K. McGuffie, W. L. Ecklund, P. E. Johnston, and K. S. Gage, 2001: Boundary layer development over a tropical island during the Maritime Continent Thunderstorm Experiment. *J. Atmos. Sci.*, **58**, 2163–2179, https://doi.org/10.1175/1520-0469(2001)058<2163:BLDOAT>2.0.CO;2.

Stankov, B. B., E. R. Westwater, and E. E. Gossard, 1996: Use of wind profiler estimates of significant moisture gradients to improve humidity profile retrieval. *J. Atmos. Oceanic Technol.*, **13**, 1285–1290, https://doi.org/10.1175/1520-0426(1996)013<1285:UOWPEO>2.0.CO;2.

Thurai, M., E. Deguchi, T. Iguchi, and K. Okamoto, 2003: Freezing height distribution in the tropics. *Int. J. Satell. Commun. Networking*, **21**, 533–545, https://doi.org/10.1002/sat.768.

Ulaby, F. T., R. K. Moore, and A. K. Fung, 1981: *Microwave Remote Sensing Fundamentals and Radiometry*. Vol. I, *Microwave Remote Sensing: Active and Passive*, Addison-Wesley, 452 pp.

Wakasugi, K., A. Mizutani, M. Matsuo, S. Fukao, and S. Kato, 1986: A direct method for deriving drop-size distribution and vertical air velocities from VHF Doppler radar spectra. *J. Atmos. Oceanic Technol.*, **3**, 623–629, https://doi.org/10.1175/1520-0426(1986)003<0623:ADMFDD>2.0.CO;2.

White, A. B., D. J. Gottas, E. T. Strem, F. M. Ralph, and P. J. Neiman, 2002: An automated brightband height detection algorithm for use with Doppler radar spectral moments. *J. Atmos. Oceanic Technol.*, **19**, 687–697, https://doi.org/10.1175/1520-0426(2002)019<0687:AABHDA>2.0.CO;2.

Williams, C. R., W. L. Ecklund, and K. S. Gage, 1995: Classification of precipitating clouds in the tropics using 915-MHz wind profilers. *J. Atmos. Oceanic Technol.*, **12**, 996–1012, https://doi.org/10.1175/1520-0426(1995)012<0996:COPCIT>2.0.CO;2.

——, ——, P. E. Johnston, and K. S. Gage, 2000: Cluster analysis techniques to separate air motion and hydrometeors in vertical incident profiler observations. *J. Atmos. Oceanic Technol.*, **17**, 949–962, https://doi.org/10.1175/1520-0426(2000)017<0949:CATTSA>2.0.CO;2.

Wilson, J. W., and E. A. Brandes, 1979: Radar measurement of rainfall—A summary. *Bull. Amer. Meteor. Soc.*, **60**, 1048–1060, https://doi.org/10.1175/1520-0477(1979)060<1048:RMORS>2.0.CO;2.

Zhang, C., M. McGauley, and N. A. Bond, 2004: Shallow meridional circulation in the tropical eastern Pacific. *J. Climate*, **17**, 133–139, https://doi.org/10.1175/1520-0442(2004)017<0133:SMCITT>2.0.CO;2.

Zhang, J., and Coauthors, 2011: National Mosaic and Multi-Sensor QPE (NMQ) system: Description, results, and future plans. *Bull. Amer. Meteor. Soc.*, **92**, 1321–1338, https://doi.org/10.1175/2011BAMS-D-11-00047.1.